

AMERICAN UNIVERSITY OF BEIRUT

OPTICAL PROPERTIES OF PULSED LASER
DEPOSITED MANGANESE OXIDE THIN
FILMS DETERMINED BY INFRARED
SPECTROSCOPY

by

RIM ASSEM IBRAHIM

A thesis
submitted in partial fulfillment of the requirements
for the degree of Master of Science
to the Department of Physics
of the Faculty of Arts and Sciences
at the American University of Beirut

Beirut, Lebanon
September 2021

AMERICAN UNIVERSITY OF BEIRUT

OPTICAL PROPERTIES OF PULSED LASER
DEPOSITED MANGANESE OXIDE THIN
FILMS DETERMINED BY INFRARED
SPECTROSCOPY

by
RIM ASSEM IBRAHIM

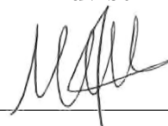
Approved by:



Dr. Malek Tabbal, Professor

Advisor

Physics



Dr. Michel Kazan, Associate Professor

Member of Committee

Physics



Dr. Sara Najem, Assistant Professor

Member of Committee

Physics

Date of thesis defense: September 02, 2021

Acknowledgements

In the name of Allah, the Most Gracious, the Most Merciful. Foremost, special gratitude goes to my mother, Hala, who has always been a source of support and love: thank you for believing in me. My beloved husband, Ali, for his sincere love, understanding, encouragement and patience through the most difficult stages of my academic years and my adorable son, Mohammad, who provides unending inspiration.. To my sister Rana, thank God for having you in my life. Special thanks to my dear Father Assem, who made me fond of science, my Ante Noha, and my soul mate Marwa Ibrahim.

I would like to send out special thanks to my advisor, Dr. Malek Tabbal, without whom this work would not have been accomplished. Moreover, I would like to express my gratitude to my committee members, Dr. Michael Kazan and Dr. Sara Najem, whose comments provided me with the theoretical aspects needed in this work.

I send my gratitude to all my colleagues Marwa, Kafa, Rola, Fatima, Zainab, Hassan and Mohamad Hadi. They have greatly enriched my education.

Thank you all for making my stay at AUB a valuable experience. At last but not least, special thanks for the chairperson, Jihad Touma for his help and support.

An Abstract of the Thesis of

Rim Assem Ibrahim for Master of Science
Major: Physics

Title: Optical Properties Of Pulsed Laser Deposited Manganese Oxide Thin Films Determined By Infrared Spectroscopy

Despite recent advances in nonlinear optical techniques for examining elementary excitations in semiconductors, infrared spectroscopy remains an attractive approach to nondestructive and quantitative measurement of relevant optoelectronic properties of materials, because of it is readily available as an experimental technique and that relatively simple theories can be used to describe the material's response to an infrared wavelength excitation. The optical and electronic behavior of semiconductors are determined by two major properties particularly energy gap and refractive index, the determination of which is necessary in the design of optoelectronic devices. In this work, we use fourier-transform infrared spectroscopy in reflective mode for the optical characterization of the manganese oxide thin films synthesized on silicon substrates using Pulsed Laser Deposition, under different experimental operating conditions, such as deposition temperature and pressure. The IR reflectivity measurements are analyzed by combining the Kramers-Kronig conversion theorem with the Fresnel equations for the reflectivity of a multilayer structure. The technique used allowed to separate the dielectric properties of the substrate from the dielectric properties of the thin films. The results obtained show that the index of refraction of the films depends on growth conditions and in some instances, high values of the index of refraction in the infrared region can be obtained. This result paves the way for interesting technological applications for these films as waveguides and other nanophotonic devices.

Contents

Acknowledgements	v
Abstract	vi
1 Introduction	1
2 ELECTROMAGNETIC WAVES IN SEMICONDUCTORS	3
2.1 Electromagnetic Waves	3
2.1.1 Electromagnetic waves in free space	3
2.1.2 Electromagnetic waves in semiconductors	4
2.2 Manganese Oxide	7
3 EXPERIMENTAL TECHNIQUES	10
3.1 Pulsed-Laser Deposition	10
3.1.1 Excimer Laser	11
3.1.2 Mechanisms of PLD	11
3.1.3 Remote Plasma Assisted PLD for Oxide Growth	12
3.1.4 PLD Experimental Setup	13
3.1.5 Remote Microwave-Plasma Source	14
3.2 Surface Profilometry	15
3.3 Characterization Method Using FT-IR Spectroscopy	15
3.3.1 Infrared Spectroscopy	15
3.3.2 Fourier Transform Infrared Spectroscopy	16
3.3.3 Extracting the spectrum from raw data	18
3.3.4 Experimental Setup	19
4 THEORETICAL STUDY	21
4.1 Kramers-Kronig Analysis	21
4.2 Fresnel Theory	24
4.2.1 Fresnel Equations	25
4.2.2 Fresnel Equations for P-polarization	26
4.2.3 Fresnel Equations for s-polarization	27
4.3 Transfer Matrix Method	27

4.3.1	Transfer Matrix for a single layer-film on a substrate . . .	28
4.3.2	Transfer Matrix for a multi-layer thin film	34
4.4	Description of the Analytical Model	38
5	RESULTS AND DISCUSSIONS	40
5.1	Measurements	40
5.1.1	Measurements for the samples grown at different temperature	42
5.1.2	Measurements for the samples grown at different deposition pressure	45
5.1.3	Measurements for the samples grown at different plasma power	47
5.1.4	Measurements for the samples grown at different laser energy	49
6	CONCLUSION AND FUTURE WORK	54
6.1	FUTURE WORK	55
A	Abbreviations	56
	Bibliography	57

List of Figures

2.1	<i>MnO</i> phase stability diagram	8
3.1	PLD system	13
3.2	Schematic diagram of experimental setup in PLD	13
3.3	Michelson Interferometer Scheme	19
4.1	s polarization	24
4.2	p polarization	25
4.3	Reflection and Transmission at interfaces	27
4.4	Single-layer film on substrate	28
4.5	Field vectors of incident, reflected and transmitted waves in p-polarization	29
4.6	Field vectors of incident, reflected and transmitted waves in s-polarization	29
4.7	The reflectance and transmission through a multi-layer semiconductor	34
4.8	Table sample for the values of n and k	38
5.1	Refractive index spectrum as a function of excitation wavelength	41
5.2	Real part of the dielectric function as function of ω for thin film synthesized at different temperature	42
5.3	Imaginary part of the dielectric function as function of ω for thin film synthesized at different temperature	44
5.4	Real part of the dielectric function as function of ω for thin film synthesized at different pressure	45
5.5	Imaginary part of the dielectric function as function of ω for thin film synthesized at different pressure	46
5.6	Real part of the dielectric function as function of ω for thin film synthesized at different plasma power	47
5.7	Imaginary part of the dielectric function as function of ω for thin film synthesized at different plasma power	48
5.8	Real part of the dielectric function as function of ω for thin film synthesized at different laser energy	49
5.9	Imaginary part of the dielectric function as function of ω for thin film synthesized at different laser energy	50

5.10	Reflectivity measurements as function of ω for sample M13	51
5.11	Reflectivity measurements as function of ω for sample M13	52

List of Tables

3.1	Samples synthesized using Pulsed Laser Deposition	15
-----	---	----

Chapter 1

Introduction

Achievements of new functions in advanced optical devices are becoming increasingly dependent on the availability of new functional materials [16]. Besides, with the advent of recent technologies, novel semiconductors rich in their optoelectronic properties encounter a wide range of applications in optical, electronic and optoelectronic devices such as light emitting diodes (LED), laser diodes (LD), integrated circuits (IC), photo detectors (PD), nanotechnology, heterostructure lasers and optical modulators operating in mid infra-red regions ($2 - 5 \mu m$) [19] [25]. The optical and electronic behaviour of semiconductors are determined by two major properties particularly energy gap and refractive index. Generally, the energy gap is determined by the threshold of photon absorption of a semiconductor while refractive index is a measure of transparency to the incident photon.

It is needless to affirm that, a proper design of optoelectronic device requires a detailed information about the refractive indices of materials. Besides, high-index dielectric materials are in great demand for nanophotonic devices and applications, from ultrathin optical elements to metal-free sub-diffraction light confinement and wave guiding.

In 1935, quickly after moderate sized artificially grown crystals of magnesium oxide became available, two papers were published handling with the optical properties of this material [24] [3]. In this work, the infrared index of refraction and the infrared dielectric function of manganese oxide are determined using a numerical technique based mainly on the reflectivity measurements using Fourier Transform Infrared Spectroscopy (FT-IR). The manganese oxides thin films used in this research work are synthesized using Pulsed-Laser Deposition (PLD). After our measurements and calculations, we find out that our synthesized samples are of high index of refraction in the infrared region. Thus, our samples are of great interest as they can be used in several applications.

In this dissertation, we will start by the theoretical background of the electromagnetic waves in semiconductors and of manganese oxides, the samples used. Then, we will display our experimental techniques used in this work: The Pulsed-

Laser Deposition (PLD) and Fourier Transform Infrared Spectroscopy (FT-IR). Later on, the numerical technique used in this work is explained in details. Finally, we will show our results and discuss them.

Chapter 2

ELECTROMAGNETIC WAVES IN SEMICONDUCTORS

2.1 Electromagnetic Waves

James Clerk Maxwell published the unified theory of electricity and magnetism in 1873 by presenting previously established experimental findings from Coulomb, Gauss, Ampere, and Faraday and by including the idea of displacement current. The claim consists of four simple equations, called the Equations of Maxwell. Maxwell's equations are one example of the postulate that fundamental laws of physics should be invariant with respect to changes from one inertial frame to another via a Lorentz transformation. What is interesting about these equations is that they are independent on the material medium. Maxwell's Equations can be in two forms, either differential or integral form. In understanding the electromagnetic field intensities at each point in the given space, the differential form is effective. The integral structure, on the other hand, is useful in describing the physical principles underlying it.

Particularly, in researching the bandgap and phonons, the electromagnetic radiation-matter interaction can be described using the classical impact of an oscillating electric field on a charge or using the quantum mechanical effect. In this chapter, we will begin by presenting the interaction's classical approach and then move to the quantum approach.

2.1.1 Electromagnetic waves in free space

Maxwell's Equations are the key tools in describing basic electromagnetic behavior. In free space, their solutions describe undamped transverse waves consisting of perpendicular oscillating magnetic and electric fields that propagate at constant speeds of light. The interaction between the electromagnetic field and the charges produces damped waves within the solid as they transfer energy to the

solid. The propagation wave speed is not constant and depends on the frequency. Incorporated in Maxwell's Equations is the full classical explanation of light:

$$\begin{aligned}
 \nabla \times E &= -\frac{\partial B}{\partial t} \\
 \nabla \times H &= j + \frac{\partial D}{\partial t} \\
 \nabla \cdot D &= \rho \\
 \nabla \cdot B &= 0
 \end{aligned}
 \tag{2.1}$$

such that:

- E: Electric Field
- B: Magnetic Field
- D: Displacement Vector
- H: Magnetic Field Strength
- ρ : Charge Density
- j: Current Density

2.1.2 Electromagnetic waves in semiconductors

Semiconductors, unlike free space, contain both free and binding charges where the free charges are the conduction electrons and the holes of the valence band in a semiconductor. In the lattice structure, which involves the host crystal and the inner electrons that are closely localized at the atomic cores, the bound charges are coated.

Therefore, because of the free and bound charges' polarizability, Maxwell's Equations are influenced by the current and charge density. Polarization P, which is the dipole moment per unit volume, is provided by bound crystal charges. It is aligned and proportional to the outside electric field E in a homogeneous linear and isotropic medium as shown in the equation below where, ϵ_0 is the electric permittivity in free space and the susceptibility of the material is represented by χ :

$$P = \epsilon_0 \chi E \tag{2.2}$$

We will present now the constitutive relations of an electromagnetic medium which relate D, the electric displacement of the medium, to its electric field E :

$$\begin{aligned}
 D &= \epsilon_0 E + P \\
 &= \epsilon_0 (1 + \chi) E \\
 &= \epsilon_0 \epsilon_{lattice} E
 \end{aligned}
 \tag{2.3}$$

where $\epsilon_{lattice} = (1 + \chi)$ is the lattice frequency-dependent dielectric response.

Consequently, the current in the material will flow because of the applied electrical field. The proportionality between the current density j and the electric field E is defined by Ohm's Law:

$$j = \sigma(\omega)E \quad (2.4)$$

Knowing that $\sigma(\omega)$ is the material's electric conductivity.

Now substitute Eq. 2.3 and Eq. 2.4 in the Maxwell's equations 2.1, we get the following relation:

$$\nabla^2 E - \nabla(\nabla \cdot E) = \epsilon_{lattice} \epsilon_0 \mu_0 \frac{\partial^2 E}{\partial t^2} + \sigma \mu \frac{\partial E}{\partial t} \quad (2.5)$$

Let

$$E = E_0 e^{i(kz - \omega t)} \quad (2.6)$$

be a plane wave solution defined by: the wave's amplitude by E_0 , the angular frequency ω , and the wave vector k :

$$\begin{aligned} k &= \frac{2\pi}{\lambda} \\ &= \frac{\omega}{v} \\ &= \frac{n\omega}{C} \end{aligned} \quad (2.7)$$

Where

- λ : Medium's wavelength
- v : Wave's speed
- n : Index of refraction
- C : Speed of light

Consequently, substitute the solution 2.6 in Eq. 2.5 to get:

$$k^2 - k(k \cdot E) = \epsilon_{lattice} \epsilon_0 \mu_0 \omega^2 E + i\sigma \mu_0 \omega E \quad (2.8)$$

$$\epsilon(\omega) = \epsilon_{lattice}(\omega) + i \frac{\sigma(\omega)}{\epsilon_0 \omega} \quad (2.9)$$

We define $\epsilon(\omega)$ to be the total dielectric response function. Where in the linear limit $\epsilon(\omega)$ is the central quantity defining the interaction between the electromagnetic wave and the semiconductors.

Accordingly, Eq. 2.8 can be written as a function of $\epsilon(\omega)$:

$$k^2 - k(k \cdot E) = \omega^2 \epsilon(\omega) \epsilon_0 \mu_0 E \quad (2.10)$$

Now the electric field E is expressed in terms of its longitudinal and transverse components:

$$E = E_t \hat{t} + E_k \hat{k} \quad (2.11)$$

where

- \hat{t} : Unit vector in the x-y plane perpendicular to the direction of propagation
- \hat{k} : Unit vector along with k

Writing Eq. 2.10 using the decomposed equation of electric field 2.11, we get:

$$\left(\frac{\omega^2}{C^2} \epsilon(\omega) - k^2\right) E_t \hat{t} + \frac{\omega^2}{C^2} \epsilon(\omega) E_k \hat{k} = 0 \quad (2.12)$$

Since Eq. 2.12 is linearly independent, each term should be equal zero to satisfy the equation. Thus, to find k , the first term of Eq. 2.12 should be equal to zero:

$$k^2 = \frac{\omega^2}{C^2} \epsilon(\omega) \quad (2.13)$$

Given the complex refractive index:

$$n^* = n + ik \quad (2.14)$$

The equation of the wave vector k 2.7 can be generalized to the absorbing medium and can be written as a function of n^* :

$$\begin{aligned} k &= \frac{n^* \omega}{C} \\ &= (n + ik) \frac{\omega}{C} \end{aligned} \quad (2.15)$$

Also, after inserting Eq. 2.15 in the wave solution Eq. 2.6, it becomes:

$$E(z, t) = E_0 e^{-\frac{k\omega z}{C}} e^{i\left(\frac{\omega n z}{C} - \omega t\right)} \quad (2.16)$$

The physical sense of the refractive index and the complex wave-vector are described by Eq. 2.16. It indicates that wave propagation is related to the real part of n^* while the imaginary part of n^* , k the extension coefficient, is related to an exponential decay of the wave as it reaches the medium.

The relation between the complex refractive index n^* and the total dielectric function $\epsilon(\omega)$ can be found by the combination of Eq. 2.15 and Eq. 2.13:

$$n^* = \sqrt{\epsilon(\omega)} \quad (2.17)$$

Hence, $\epsilon(\omega)$ can be written as a function of the real and imaginary parts:

$$\begin{aligned}\epsilon(\omega) &= n^{*2} \\ &= \epsilon_1 + i\epsilon_2\end{aligned}\tag{2.18}$$

Now, using Eq. 2.13, we can extract the relations between the real and imaginary parts of n^* and $\epsilon(\omega)$:

$$\begin{aligned}\epsilon_1 &= n^2 - k^2 \\ \epsilon_2 &= 2nk \\ n &= \frac{1}{\sqrt{2}}\sqrt{\epsilon_1 + |\epsilon|} \\ k &= \frac{1}{\sqrt{2}}\sqrt{-\epsilon_1 + |\epsilon|}\end{aligned}\tag{2.19}$$

Consequently, by its frequency-dependent dielectric function, the microscopic optical response of semiconducting materials, defined by the refractive index and extinction coefficients, can be controlled. When the reflectance spectroscopy of the semiconductor is taken into account, the measurements and calculations will be clearer.

In this work, we are interested in Manganese Oxide thin films deposited on silicon substrate. The aim of the presented work, it to develop a numerical technique to retrieve the dielectric property of Manganese Oxide using reflectivity measurement of unpolarized light. We also want to check how do the deposition parameters affect the dielectric properties of the different Manganese Oxide microstructure.

2.2 Manganese Oxide

Due to their possible technical applications and appealing physical properties, Manganese Oxides have attracted considerable interests in thin-film sciences. Across several oxidation states: Mn^{2+} , Mn^{3+} , and Mn^{4+} manganese cations can exist. These manganese cations contribute to the crystallization of the respective oxides into stable phases, of which MnO, Mn_3O_4 , Mn_2O_3 , and MnO_2 are the most widely recognized.

Figure 2.1 presents the manganese-oxide phase diagram [15]:

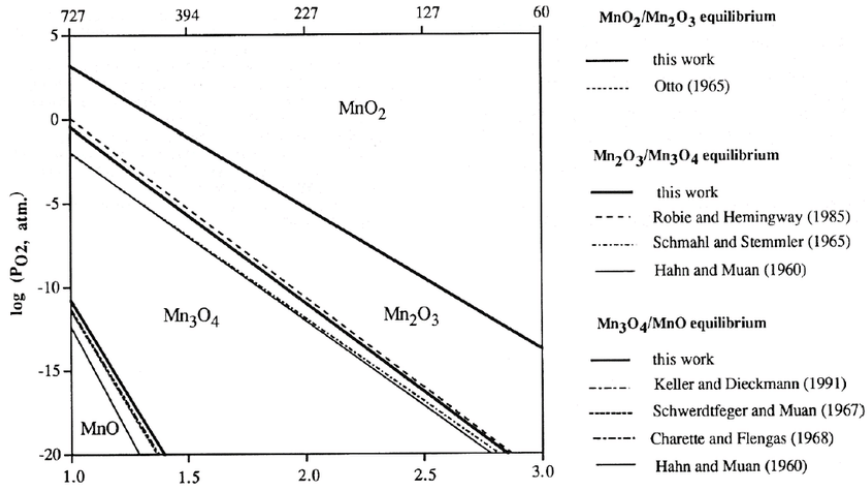


Figure 2.1: *MnO* phase stability diagram

Figure 2.1 illustrates the presence of various phases of manganese oxide, that have different physical and chemical properties including their structures, crystal consistency and chemical stoichiometry. It is assumed that each of the above MnO phases mentioned will be stable in a well-defined pressure and temperature area (where the pressure log lies on the y-axis and temperature lies on the x-axis). Experimentally, the various lines dividing the phases were found [10] where the transition from one phase to another can be accomplished by appropriate temperature and oxygen pressure changes.

Manganese Oxides, as semiconductors, show interest in various applications: as a part of dry cell batteries [17], promising electrode materials for electrochemical capacitors [31], [27], and for several chemical applications as catalysts for oxidation of CO and CO_2 . Manganese Oxides also play a significant role as electrolyte components for lithium cells [20], biocatalysts in microbial fuel cell [8], catalysts for water treatment[9] and efficient removals of Co^{2+} and Sr^{2+} from aqueous solutions [14]. They are also used as gas sensors[4],[6]. Moreover, their novel mesoporous structure has been attractive for large scale applications in mobile equipment [28], and they have appealed to comprehensive attention in the field of anticancer applications [30].

Manganese oxides, with their different phases, are one of the most important groups of materials in science. Mn_3O_4 , alluded to as hausmanite, contains a spinel structure with tetragonal twisting prolonged along the c axis (space group I41/amd) [2]. AB_2O_4 is the common equation of the spinel structure where A atoms possess the tetrahedral sites and B atoms occupy the octahedral sites that are presented within the unit cell. By comparison to this structure, manganese cations are localized as takes after: On the tetrahedral A positions, Mn_{2+} is positioned while Mn_{3+} occupies the octahedral B locations

with the lattice parameters $a = b = 5.762 \text{ \AA}$ and $c = 9.470 \text{ \AA}$ [13]. At room temperature and pressure, this tetragonal structure is stable whereas Mn_3O_4 undergoes at high temperature ($T = 1160^\circ C$) a Jahn-Teller transition (JTT) followed by a major lattice deformation that gives rise to a cubic structure. The development of an orthorhombic phase results in higher pressure (10GPa) and temperature($900^\circ C$)[11]. Mn_3O_4 is classified at room temperature as a weak conductor with resistivity on the order of 10^7 ohm-cm at room temperature [5]. The electrochromic properties of this material were revealed in a study on Mn_3O_4 thin films grown by chemical vapor deposition, where the films displayed a shift in optical absorption when an electric field was applied[18].

Another interesting phase of manganese oxides is dimanganese trioxide, Mn_2O_3 . Mn_2O_3 has a crystal unit cell that comprises 32 ions of Mn^{3+} and 48 ions of O^{2-} . This compound goes from an orthorhombically distorted bixbyite defined by the $Pcab$ space group to an undistorted cubic bixbyite with $Ia\bar{3}$ symmetry at a temperature of 302K [12],[7]. Magnetic structure studies show that $\alpha - Mn_2O_3$ at T_N 90K is para-magnetic and at lower temperatures becomes anti-ferromagnetic [21].

Another manganese oxide form is MnO, known as manganous oxide, which has the same crystal structure as NaCl with a lattice constant of $a = 4.445 \text{ \AA}$. At room temperature, it is para-magnetic and undergoes a first-order transition at 118 K to an anti-ferromagnetic phase [29].

In this research work, our main goal is to study the infrared dielectric function of manganese oxide thin film deposited on silicon substrate using Pulsed Laser Deposition.

Chapter 3

EXPERIMENTAL TECHNIQUES

This chapter describes the experimental setup of the technique of Pulsed Laser Deposition (PLD) used for the growth of thin films of manganese oxide and the various experimental techniques used for the characterization of the films grown. First, Remote Plasma Assisted Pulsed Laser Deposition (RPA-PLD) along with the various parameters of deposition is described.

For the aim of finding the dielectric function of the manganese oxide thin films deposited by PLD, Fourier Transform Infrared Spectroscopy (FTIR) is performed. We measure the film thickness using Stylus Profilometer.

3.1 Pulsed-Laser Deposition

PLD has evolved rapidly as a very promising technique used to produce a wide range of films. This is because of the simplicity and versatility of the method that allows the growth of complex multi-layered structures under ultra-high vacuum conditions and controllable pressures and temperatures. In microelectronic devices and optical coatings, PLD has been chosen as the technique for the growth of oxides that are considered essential for technological breakthroughs.

The technique of pulsed laser deposition (PLD) uses short-last laser pulses of high power to ablate a solid target. The laser energy evaporates material from the surface of the target, creating a transient, highly luminous plasma plume composed of ablated species, expanding and condensing on a substrate placed in front of the target, thus inducing film growth. In the presence of a background gas such as oxygen or nitrogen that can react chemically with the ejected species or even an inert gas such as argon to alter plume dynamics, the film can be produced. The key deposition conditions that significantly influence the physical process of PLD are: laser parameters, target material properties, background pressure, and substrate temperature. In what follows, the main characteristics of

PLD and the basic mechanisms that come into play during film growth will be described briefly.

3.1.1 Excimer Laser

The excimer is an unstable diatomic molecule of inert gas and halogen, emitting a photon in the UV range when decaying. The laser used in our work is the KrF laser with emitted wavelength of 248nm. As most target materials have a high absorption coefficient and a limited penetration depth, this value in the UV range is suitable for PLD thin-film growth.

3.1.2 Mechanisms of PLD

While it is very easy to set up the PLD framework, the physical theory of PLD is very complicated. It requires the physical phase of the interaction of the laser material with the impact of the high-power pulsed laser on the solid target, the creation of the plasma plume with high-energy species, and the transition to the heated substrate surface of the ablated material via the plasma plume.

The process of thin film formation by PLD are generally divided into three sections:

1. Light-material interaction: when the laser radiation is absorbed by the target's surface area, electromagnetic radiations in the form of plasmons and unbound electrons are immediately transformed into electronic excitation. Within a few picoseconds, the excited electrons transfer their energy to the lattice and heating of the absorption layer begins.
2. Plasma generation and expansion: the laser energy should be sufficiently high for substantial surface evaporation and material removal from the target's surface. In this scenario, there is surface evaporation within a portion of the pulse of ns. The vapor is hot enough, and some of the atoms are ionized within the vapor. This vapor will further absorb energy from the remaining pulse; a completely ionized plasma will therefore be formed in an area called the Knudsen layer near the target surface.
3. Film growth: the growth of films and their quality depend on the temperature of the substrate, the rate of deposition, and the expanding species' kinetic energy. It is also possible to include the effects of vacuum efficiency and the background gas as fundamental parameters that affects the growth. The deposition parameters should be set in such a way that the plume tip hits the substrate surface in order for film growth to take place. The high-energy species expelled impinge on the surface of the substrate and can cause different types of substrate damage. Some of the surface atoms are

sputtered by these energetic species and a collision region is formed between the incident flow and the sputtered atoms. Film grows after the development of a thermalized zone. The area serves as a source of particle condensation. Thus, when the rate of condensation is greater than the rate of particles provided by the sputtering, the state of thermal equilibrium can be easily achieved and the film grows on the surface of the substrate.

3.1.3 Remote Plasma Assisted PLD for Oxide Growth

For oxide film growth by PLD, the presence of O_2 gas in the reaction chamber is important, where chemical reactions between the ambient gas and the expelled species can promote the absorption of oxygen into the deposited layers. However, an abundant presence of oxygen in the film that may not be adequately supplied by working at high O_2 pressure is needed when finding a particular phase characterized by a high oxidation state of a certain metal. The connection of the PLD system to a plasma source producing reactive oxygen species consisting primarily of vibrationally excited molecules and dissociated oxygen atoms satisfies this requirement. This technique, known as Plasma Assisted PLD (PA-PLD), has been shown to improve the consistency of the films grown and to stabilize unattainable metastable phases by traditional PLD. The creation of oxygen-excited species that are much more reactive than O_2 molecules encourages the further incorporation of oxygen into the rising layers. Thus allows the chemical composition and crystalline nature of the deposited layers to be better regulated. A microwave (MW), radio frequency (RF), and direct current (DC) discharge may be used to generate ions along with excited atomic and molecular species. A remote plasma is generated when these excited species are guided by the gas flow from the discharge zone to the area where the deposition process takes place and the resulting process is called Remote Plasma Assisted PLD (RPA-PLD).

3.1.4 PLD Experimental Setup

Using our "SURFACE" workstation, shown in Figure 3.1, manganese oxide thin films were synthesized.

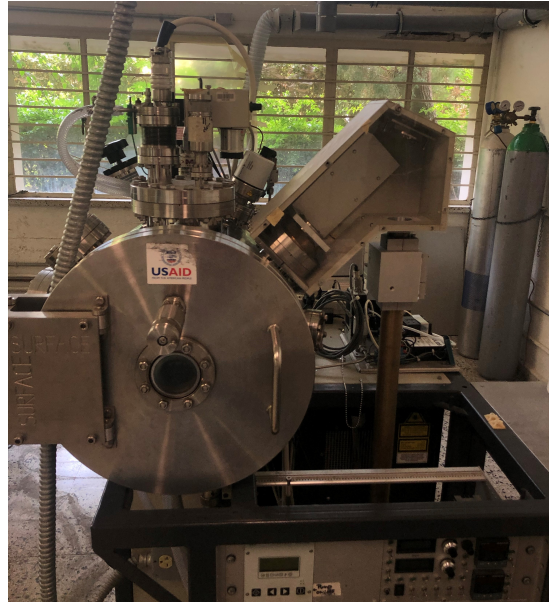


Figure 3.1: PLD system

Figure 3.2 represents a schematic diagram for a typical PLD experimental setup.

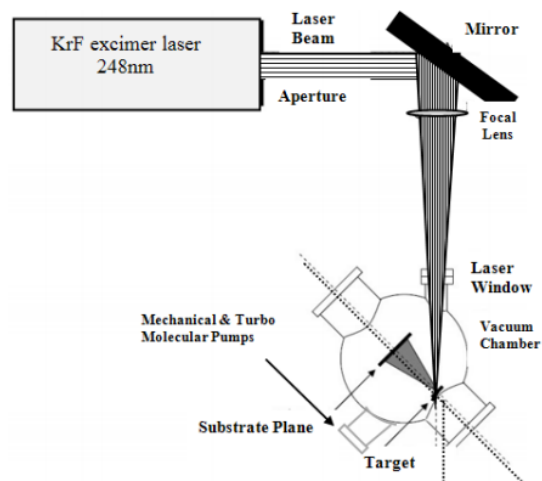


Figure 3.2: Schematic diagram of experimental setup in PLD

It consists mainly of a high vacuum deposition chamber that achieves a base pressure of 10^{-7} mbar (7.5×10^{-8} mTorr) coupled to a turbomolecular and diaphragm pump-based pumping unit. It also includes an optical device based on a KrF excimer laser with a wavelength of 248 nm, a pulse period of 20 ns with an adjustable repetition rate (1-10 Hz) and a laser energy of up to 600 mJ. The repetition rate is set at 10 Hz during deposition, while the laser energy varies between 200 and 500 mJ. The target is placed on rotary drives that facilitates the rotation in order to maintain homogeneous consumption of the target. Thin films of Manganese oxide have been deposited by ablation of a pure MnO target (99.9 %). Films are grown on single crystal substrates of Si (100) that were chemically treated prior to each deposition cycle. The substrate holder comprises a thermocouple for temperature readings and a heater that allows complete regulation of the deposition temperature up to 950 °C. The temperature ranged from 25 to 650 °C in our experiment. Deposition runs are performed in an oxygen gas or remote oxygen plasma chemically reactive atmosphere produced by a microwave plasma source connected to the deposition chamber.

3.1.5 Remote Microwave-Plasma Source

The source of plasma consists of two primary parts:

1. The MW generator wave guide with R26-coaxial transformer, as well as the sliding elements of the tuning and the power generator.
2. The vacuum quartz tube in which the plasma is created by connecting microwaves to the flowing gas. This tube, which is placed directly on the deposition chamber, guarantees the transport of the excited species into the chamber with the gas flow to the area where the deposition process takes place to form what is usually referred to as remote plasma.

In order to avoid overheating of the device, water and air cooling of the plasma source is required. The plasma power was set to 400W during deposition with plasma activation, a value obtained by minimizing the reflected power to a limit.

As mentioned, the samples used in this work are manganese oxide thin films deposited on silicon substrate. Table 3.1 shows the conditions used to obtain a MnO_2 thin film.

Sample	Thickness	Pressure	Temperature	Plasma Power	Laser Energy
T3	840	100	500	350	220
T4	800	100	250	350	220
T14	750	100	500	400	470
T15	930	50	500	400	470
T8	880	250	500	400	500
T9	850	250	500	0	500
T1	990	100	500	0	328
M13	770	100	500	0	200

Table 3.1: Samples synthesized using Pulsed Laser Deposition

Where the units of: thickness: nm, temperature $^{\circ}C$, pressure: mbarr, plasma Power: W , and Laser Energy: mJ.

The synthesized samples are divided into 4 groups:

- Group 1: Samples T3 and T4 are grown at different temperature
- Group 2: Samples T14 and T15 are grown at different pressure
- Group 3: Samples T8 and T9 are grown at different plasma power
- Group 4: Samples T1 and M13 are grown at different laser energy

3.2 Surface Profilometry

Surface profilometry is a mechanical technique used to determine film thickness by detecting a stylus's mechanical motion as it traces a film-substratum phase topography. The phase is done before deposition by masking a small region of the sample.

3.3 Characterization Method Using FT-IR Spectroscopy

3.3.1 Infrared Spectroscopy

Herschel has discovered IR radiation in 1800. Then, the applications on IR spectroscopy rises in material sciences by 1900 when the spectra for 52 compounds were recorded relating molecular structure with absorption bands by

Abney and Festing. IR spectroscopy also known as vibrational spectroscopy measures matter-infrared radiation interaction dealing with the infrared portion of the electromagnetic spectrum that lies on its low energy side (lower frequency and larger wavelength than visible light). The method of infrared spectroscopy gives an infrared spectrum utilizing a spectrometer used for the identification of chemical substances or functional groups by measuring absorption, emission, transmission and reflection.

IR absorption is defined by the transition of a molecule from the ground state to a vibrationally excited state using the absorption of an infrared photon with energy equals to the difference between the energies of the two states. Whereas in IR emission a photon is emitted by a molecule during its transition from the excited to the ground state. Therefor, IR infrared spectroscopy identifies characteristic vibrational bands of bonded units to give chemical information about the molecular structure of a material.

In IR transmission spectroscopy, part of the IR radiation transmits through the samples and the other is absorbed which gives a spectrum indicating the molecular absorption and transmission, and thus generating a molecular fingerprint of the sample. Whereas, in IR reflection spectroscopy, the technique we are dealing with in our work, the change in the reflectance spectrum is measured for thin films deposited on reflective substrates. The infrared spectrum for each molecular structure is unique, as each molecule has a specific combination of atoms. Thus, infrared spectroscopy can serve in the study of different types of material.

3.3.2 Fourier Transform Infrared Spectroscopy

Fourier-transform infrared spectroscopy (FTIR) is a technique for obtaining the absorption or emission spectrum of a solid, liquid, or gas in the infrared. High-resolution spectral data is obtained simultaneously by an FTIR spectrometer over a large spectral spectrum. The term Fourier-transform infrared spectroscopy stems from the fact that in order to convert raw data into the actual spectrum, a Fourier transform (a mathematical process) is required. The aim of absorption spectroscopy techniques is to measure how much light at each wavelength a sample absorbs. The easiest way to do this is to shine a monochromatic light beam at a sample, determine how much of the light is absorbed, and repeat for each different wavelength, this is called the "dispersive spectroscopy" process. A less intuitive way of collecting the same knowledge is Fourier-transform spectroscopy. This technique shines a beam containing several frequencies of light at once instead of shining a monochromatic beam of light at the sample and tests how much of the beam is absorbed by the sample. Next, the beam is altered to contain a particular frequency combination, giving a second data point. Over a short time period, this process is replicated rapidly several times. Then, a computer takes all this knowledge and works backward to decide at each wavelength what the

absorption is. Computer processing is necessary, as stated, to translate the raw data into the desired result (light absorption for each wavelength). A popular algorithm called the Fourier transform turns out to be the processing necessary.

Sample molecules selectively absorb radiation from particular wavelengths when exposed to infrared radiation, causing the dipole moment shift of the sample molecules. The vibrational energy levels of the sample molecules are then transferred from the ground to the excited state. The vibrational energy GAP defines the frequency of the absorption peak. The number of peaks of absorption is related to the molecule's vibrational freedom. The strength of the peaks of absorption is connected to the shift dipole moment and to the probability of the transition of energy levels. Therefore, one can readily obtain abundant structure knowledge from a molecule by studying the infrared spectrum. The fact that it is capable of analyzing all gas, liquid, and solid samples is what makes infrared absorption spectroscopy even more useful.

The vibrations of molecular bonds are explained by Hooke's law where two atoms within the connecting bond are treated as a simple harmonic oscillator. Thus, the spring's vibration frequency is connected to the reduced mass $\mu = \frac{m_1 m_2}{m_1 + m_2}$ of the two atoms forming the molecule and the spring constant k by the following equation:

$$\nu_{vib} = \frac{1}{2\pi} \sqrt{\frac{k}{\mu}} \quad (3.1)$$

Knowing that the infrared energy region of the electromagnetic spectrum includes the typical values of ν_{vib} which are of order $10^{14} s^{-1}$. Vibrational motion is quantized in accordance with quantum mechanics, and the mechanical solution of a quantum harmonic oscillator is as follows:

$$E_i = h\nu(n_i + \frac{1}{2}) \quad (3.2)$$

Where $n_i = 0, 1, 2, \dots$ is the vibrational quantum number.

As quantum theory describes the interaction between an atom and light, the absorbed energy of radiation is a multiple number of the energy difference between the molecular vibrational ground and excited states. Therefore, light absorption takes place when the frequency of the infrared radiation matches with the vibrational frequency of the molecule and contributes to an infrared spectrum characteristic of the molecular structure.

In addition, FTIR has achieved a substantial rise in modern software algorithms, so it is an irreplaceable instrument for quantitative analysis. What made FTIR analysis almost infinite, highly accurate and worthwhile over the dispersive infrared spectral analysis methods:

- The interferometer which results in extremely quick measurements as all the frequencies are measured simultaneously, so most FTIR measurements are made in a matter of seconds rather than several minutes.

- High signal-to-noise ratio which is proportional to the time of measurement, and the number of scans as data is obtained at the same time from all wavelengths.
- High resolution which is obtained by increasing the distance of mirror movement without the use of narrow slits.

Various types of interferometers, such as the Michelson interferometer, the lamellar grating interferometer, and the Fabry-Perot interferometer can be used in FTIR spectroscopy. The FTIR spectrometer method can be briefly explained as follows:

- The interferometer produces a signal known as an interferogram.
- The obtained signal is a record of intensity by the detector as a function of optical path difference of the two beams of the interferometer.
- Apply Fourier transform for the interferogram to get the final spectrum .

The intensity which is a function of path difference transforms as a whole to give the spectrum S which is a function of frequency ν . This is known as the inverse Fourier Transform:

$$S(\nu) = \int_{-\infty}^{\infty} I(x)e^{i2\pi\nu x} dx = F^{-1}[I(x)] \quad (3.3)$$

where the Fourier Transform is:

$$I(x) = \int_{-\infty}^{\infty} S(\nu)e^{i2\pi\nu x} d\nu = F[S(\nu)] \quad (3.4)$$

3.3.3 Extracting the spectrum from raw data

Using a computer, the interferogram $I(x)$ is transformed to the spectrum $S(\nu)$ by the inverse Fourier transform integral. Where the interferogram is decoded using Fourier transform to draw out the actual spectrum $I(\nu)$. Then, the detector collects the intensity which is a function of the path length differences in the interferometer x and wave-number ν :

$$I(x, \nu) = I(\nu)[1 + \cos(2\pi\nu x)] \quad (3.5)$$

Therefore, for every data point at a specific path length difference, the total intensity measured is:

$$I(x) = \int_0^{\infty} I(x, \nu) d\nu \quad (3.6)$$

Now, we can reach the spectrum $S(\nu)$ in terms of $I(x)$ by determining the inverse Fourier transform to get:

$$S(\nu) = 4 \int_0^{\infty} [I(x) - \frac{1}{2}I(x=0)] \cos(2\pi\nu x) dx \quad (3.7)$$

3.3.4 Experimental Setup

Most of the available Fourier transform spectrometers use Michelson interferometer, which is easy to construct and operate.

A typical Michelson interferometer consists of two perpendicular mirrors and beamsplitter.

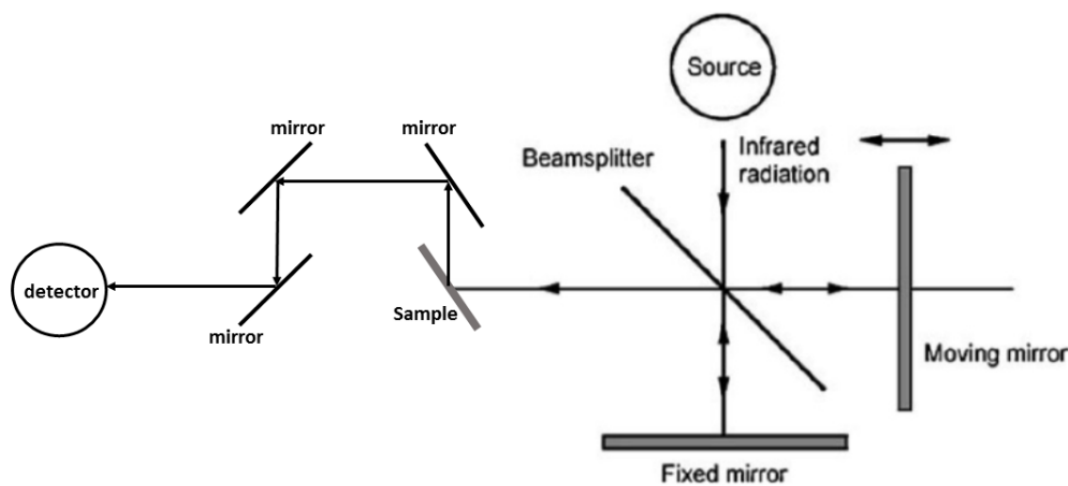


Figure 3.3: Michelson Interferometer Scheme

In frequency measurements, the benefits of using the Michelson interferometer are its high sensitivity to surface topography, ability to cover large areas with high resolution, and high accuracy. In a standard Michelson interferometer, there are a beam splitter and two perpendicular mirrors in which one of the mirrors is fixed and the other is free to move. The beam splitter is used to reflect half of the light towards the fixed mirror and transmits the other half towards the moving mirror. Then the light is reflected back toward the beam splitter where they recombine after hitting the mirrors. This recombination of light waves will lead to an interference pattern incident on the detector due to the difference in path difference. This pattern is called the interferogram, where at each data point that is a function of the location of the moving mirror, collects information about all the infrared frequencies produced from the source. Thus, the use of an interferometer enhances our measurements as all the frequencies are determined concurrently as the interferogram is obtained.

In this research work, the FTIR system is a Nicolet 4700 spectrometer from Thermo Electron Corporation in the mid-infrared range of $400\text{-}4000\text{ cm}^{-1}$. On the samples, 100 scans were performed out adjusting the resolution to cm^{-1} in

order to improve the signal-to-noise ratio. As the sample compartment is not evacuated, a relative scale is required for the absorption intensity. Before each measurement, we use a gold-coated mirror to obtain a background spectrum and this is before placing the sample. To remove the contribution of both the instrumental and environmental features to the infrared spectrum, the background signal is subtracted from the sample's spectrum. As a result, the sample is intensively responsible for all spectral features that occur in the collected spectrum. Adjustment of parameters and data collection are manipulated by OMNIC software, while the data collected is plotted and analyzed using Microcal Origin software.

Chapter 4

THEORETICAL STUDY

The main objective of this research work is to determine the dielectric property of manganese oxide thin films using reflectivity measurement of unpolarized light. In order to manipulate the dielectric properties, we use the Transfer Matrix Method which has been used to calculate the optical reflectance of multilayer structures by creating a chain of multiplied single layer-transfer matrices, accompanied by the boundary conditions of the electromagnetic fields at the interfaces of the structure. By determining the reflectance in a very abstract way, we can estimate the main optical properties of a given combination of films.

4.1 Kramers-Kronig Analysis

The main aim of this section is to find the classical Hilbert transform relations that contribute to the complex dielectric constant between the real and imaginary components of the generalized complex refractive index. Connections of this kind are mostly referred to in the literature of physics as dispersion relations. However, they are most commonly referred to as the Kramers-Kronig relations for the two functions just described, and for many related attributes. Historically, these were the first implementations in the physical sciences of the Hilbert transform principle and were discovered by Kronig (1926) and Kramers independently (1927). Hence, Kramers-Kronig (K-K) analysis is a universal method of extraction of the complex dielectric function from experimentally accessible optical quantities is developed [22].

Using specular spectrometer, spectral measurement can be achieved easily without damaging the sample. However, irregular dispersion occurs when it is applied to the measurement of a sample that is highly specular as a glassy or crystalline material and experiences absorption in the infrared region, rendering the spectrum peaks distorted to look like those of a first derivative curve. Analysis and recognition of functional groups from such a continuum is difficult. This distorted spectrum therefore needs to be transformed for analysis into an ordinary

spectrum. For that reason, the Kramers-Kronig transform is used.

The Kramers-Kronig relations are:

$$\begin{aligned}\chi_1(\omega) &= \frac{P}{\pi} \int_{-\infty}^{\infty} \frac{\chi_2(\omega') d\omega'}{\omega' - \omega} \\ \chi_2(\omega) &= -\frac{P}{\pi} \int_{-\infty}^{\infty} \frac{\chi_1(\omega') d\omega'}{\omega' - \omega}\end{aligned}\tag{4.1}$$

where given:

$$\chi(\omega) = \chi_1(\omega) + i\chi_2(\omega)\tag{4.2}$$

A complex function, such that $\chi_1(\omega)$ and $\chi_2(\omega)$ are real numbers. P is the Cauchy principle value.

For satisfying (K-K), the complex function $\chi(\omega)$ is defined such that the function $\chi_1(\omega)$ is even and the function $\chi_2(\omega)$ is odd with respect to real ω and the positions of the $\chi(\omega)$ poles are below the real axis and the function in the upper half of the complex plane is analytic. Moreover, as taken around an infinite half circle in the upper part of the complex plane, the $\int \frac{\chi(\omega)}{\omega}$ tends to zero.

Upon manipulating the real portion of $\chi(\omega) = \chi_1(\omega) + i\chi_2(\omega)$ and dividing the integral into two parts, we get:

$$\begin{aligned}\chi_1(\omega) &= \frac{P}{\pi} \int_{-\infty}^{\infty} \frac{\chi_2(\omega') d\omega'}{\omega' - \omega} \\ \chi_1(\omega) &= \frac{P}{\pi} \int_{-\infty}^0 \frac{\chi_2(\omega'') d\omega''}{\omega'' - \omega} + \frac{P}{\pi} \int_0^{\infty} \frac{\chi_2(\omega') d\omega'}{\omega' - \omega}\end{aligned}\tag{4.3}$$

Now substituting ω'' for $-\omega'$ and $\chi_2(-\omega') = -\chi_2(\omega')$ we get the following two integrals:

$$\begin{aligned}\chi_1(\omega) &= \frac{2P}{\pi} \int_0^{\infty} \frac{\omega' \chi_2(\omega') d\omega'}{\omega'^2 - \omega^2} \\ \chi_2(\omega) &= \frac{-2\omega P}{\pi} \int_0^{\infty} \frac{\chi_1(\omega') d\omega'}{\omega'^2 - \omega^2}\end{aligned}\tag{4.4}$$

Kramers Kronig transform is one of the key instruments in all media for the study of phenomena of light matter interaction as it provides constraints for checking the self-consistency of data produced by experiments or models. It also enables the inversion of optical data, i.e. data on dispersive phenomena can be calculated by translating absorptive phenomena measurements all over the entire spectrum and vice versa. Thus, the main purpose now is to relate the only experimental data extracted in our work, the reflectance $R(\omega)$, to the real and imaginary parts of the dielectric optical function.

We will express $r(\omega)$, the reflectivity coefficient (light intensity ratio), defined at the surface of a crystal in it's polar notation to be:

$$r(\omega) = \frac{E_R}{E_I} = \rho(\omega)e^{i\theta(\omega)} \quad (4.5)$$

where:

- The modulus: $\rho(\omega) = \sqrt{R(\omega)}$
- The argument: $\theta(\omega)$ is the phase difference between the reflected and transmitted rays and will be extracted from the experimental values of $R(\omega)$.

In this way, infrared spectrum analysis by Kramers-Kronig is used to derive the phase shift from the measured experimental data $R(\omega)$. To accomplish our objective of determining the complex dielectric function of the system we should provide a relation between the reflectivity coefficient $r(\omega)$ and the complex refractive index $n^*(\omega) = n(\omega) + ik(\omega)$. The corresponding relations are expressed as:

$$r(\omega) = \sqrt{R}e^{i\phi} = \frac{n_2 \cos \theta_1 - n_1 \cos \theta_1}{n_2 \cos \theta_1 + n_1 \cos \theta_1} \quad (4.6)$$

$$R = |r|^2 = r.r^* \quad (4.7)$$

The term r^* is the complex conjugate of r . The logarithmic expression of Eq. 4.7 is as follows:

$$\ln(r) = \ln(\sqrt{R}) + i\phi \quad (4.8)$$

In Eq. 4.8, \sqrt{R} and ϕ are mutually dependent according to the Kramers-Kronig equation:

$$\begin{aligned} \phi(\omega) &= -\frac{\omega P}{\pi} \int_0^\infty \frac{\ln R(\omega') d\omega'}{\omega'^2 - \omega^2} \\ \phi(\omega) &= -\frac{\omega}{\pi} \int_0^\infty \frac{(\ln R(\omega') - \ln R(\omega)) d\omega'}{\omega'^2 - \omega^2} \end{aligned} \quad (4.9)$$

By integrating by parts Eq. 4.9, we can obtain a more effective expression of the theoretical phase shift which displays the whole reflection spectrum from zero to infinite frequencies where:

$$\phi(\omega) = -\frac{1}{2\pi} \int_0^\infty \ln \frac{|\omega' + \omega|}{|\omega' - \omega|} \frac{d \ln R(s)}{d\omega'} d\omega' \quad (4.10)$$

The integral 4.10 shows that only a limited part of the entire spectrum contributes significantly to $\phi(\omega)$. Whereas, the regions with constant reflectance and those where $\ln \frac{|\omega' + \omega|}{|\omega' - \omega|}$ is very weak, such that $\omega' \gg \omega$ or $\omega' \ll \omega$, do not contribute in the integral. Consistently, significant contributions come from the neighborhood of ω_0 , where $\ln \frac{|\omega' + \omega|}{|\omega' - \omega|}$ gives a very sharp peak and from region where reflectivity shifts quickly.

4.2 Fresnel Theory

The Fresnel equations explain how light (or electromagnetic radiation in general) reflects and transmits when an interaction between various optical media occurs. Augustin-Jean Fresnel was the first to recognize that light is a transverse wave, even though no one knew that electric and magnetic fields were the "vibrations" of the wave. Polarization could be quantitatively understood for the first time, as Fresnel's equations [23] correctly predicted the different behavior of the s and p polarization waves on a material interface. When the interface between two mediums with different refractive indices (say n_1 and n_2) is reached by light, there can be both reflection and refraction of light. The Fresnel equations describe the ratios of the electric fields of the reflected and transmitted waves to the electric field of the incident wave where the magnetic fields of the waves can also be related using identical coefficients. They define not only the relative amplitude, but also the phase changes between the waves because these are complex ratios. Moreover, they presume that the interface between the media is flat and that the media is homogeneous and isotropic. Fresnel and Maxwell's equations are coherent with the treatment of light. Hence, by setting the boundary conditions of Maxwell's equations at each interface, the behavior of electromagnetic waves at the interface between two different mediums is found. Consequently, we consider the incident light to be a plane wave, which is sufficient to solve any problem because it is possible to decompose into plane waves and polarizations.

As mentioned above for two separate linear polarization elements of the incident wave, there are two sets of Fresnel coefficients:

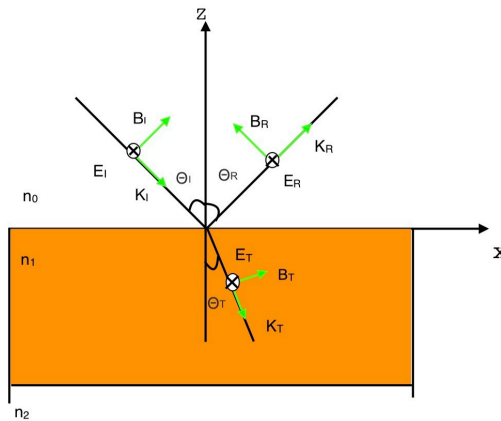


Figure 4.1: s polarization

1. S-polarization (parallel) where light's electric field is oriented perpendicular to the incidence plane, and the magnetic field is in the plane of incidence.

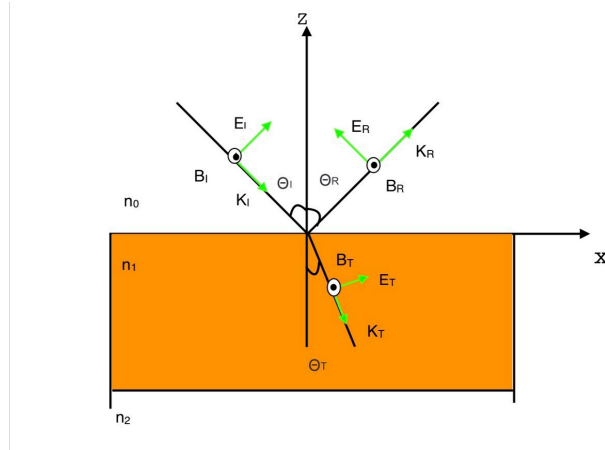


Figure 4.2: p polarization

2. P- polarization (perpendicular) where light is known to have an electric field direction parallel to the incidence plane ,and it's magnetic field is perpendicular to the incidence plane.

4.2.1 Fresnel Equations

Referring to figure(s), we can observe the incident plane wave hitting the the interface separating two media of different refractive index, n_1 and n_2 . A part of this wave is reflected and the other is transmitted through the surface. The given angles θ_I (angle of incidence) and θ_R (angle of reflection) are related using the law of reflectivity:

$$\theta_I = \theta_R \quad (4.11)$$

As well as angles θ_I and θ_T (angle of transmission) are related by Snell's law:

$$n_1 \sin \theta_I = n_2 \sin \theta_T \quad (4.12)$$

Now, by considering the electric and magnetic fields that form the electromagnetic wave presented is the Fig. 4.2/4.1 above and the laws of electromagnetism, the action of light on the interface is solved. Hence, to find the fraction of the incident power reflected from the interface, the reflectance, we should apply electric and magnetic fields' boundary conditions at the interface between n_1 and n_2 . E_R and E_T are the amplitude of the reflected and transmitted electric field respectively.

Apply Faraday's and Ampere's law to a rectangular loop mounting the surface to draw out the boundary conditions for the tangential components of electric and magnetic fields. In the manner of deriving the Fresnel's equation for parallel and perpendicular polarization, we will define the coefficient of reflection:

$$r = \frac{E_R}{E_I} \quad (4.13)$$

and the coefficient of transmission:

$$t = \frac{E_T}{E_I} \quad (4.14)$$

For solving the equations that we will derive from the boundary conditions, we should recall the Maxwell's equation that relates the electric and magnetic fields for any wave by:

$$H = \sqrt{\frac{\epsilon}{\mu}} E \quad (4.15)$$

where:

- ϵ is the electric permittivity of the material in which the light propagates
- μ is the magnetic permeability of the material in which the light propagates

Now, as $n = \sqrt{\epsilon}$ and $\mu = 1$ at optical frequency we get:

$$\begin{aligned} H_{I,R} &= n_1 E_I \\ H_T &= n_2 E_T \end{aligned} \quad (4.16)$$

4.2.2 Fresnel Equations for P-polarization

Referring to figure 4.2, the reflected and transmitted waves are of the same polarization by symmetry. Applying the tangential boundary conditions for the tangential components of electric fields that should be continuous across the boundaries, we get:

$$E_I \cos \theta_I + E_R \cos \theta_R = E_T \cos \theta_T \quad (4.17)$$

However, we get for the magnetic field which is collinear in the incident, reflected, and transmitted manner:

$$H_I - H_R = H_T \quad (4.18)$$

Combining equations 4.16 and 4.18, we get:

$$n_1(E_I - E_R) = n_2 E_T \quad (4.19)$$

Connecting equation 4.17 with equation 4.19, we get the P-polarized Fresnel equations:

$$\begin{aligned} t_p &= \frac{2n_1 \cos \theta_I}{n_1 \cos \theta_T + n_2 \cos \theta_I} \\ r_p &= \frac{n_1 \cos \theta_T - n_2 \cos \theta_I}{n_1 \cos \theta_T + n_2 \cos \theta_I} \end{aligned} \quad (4.20)$$

4.2.3 Fresnel Equations for s-polarization

On the other hand, referring to figure 4.1, the boundary conditions for the perpendicular polarization:

$$E_I + E_R = E_T \quad (4.21)$$

$$-H_I \cos \theta_I + H_R \cos \theta_I = H_T \cos \theta_T \quad (4.22)$$

This leads to the s-polarization Fresnel equations:

$$t_s = \frac{2n_1 \cos \theta_I}{n_1 \cos \theta_I + n_2 \cos \theta_T} \quad (4.23)$$

$$r_s = \frac{n_1 \cos \theta_I - n_2 \cos \theta_T}{n_1 \cos \theta_I + n_2 \cos \theta_T}$$

4.3 Transfer Matrix Method

The study of multi-layer films has gained increasing interest in recent years due to their many potential uses as optical coatings and as transparent conductive electrodes in opto-electronic devices such as flat displays, thin film transistors and solar cells [26]. As the unique optical properties of multi-layer films play an important role in the construction of thin-film solar cells' it is important for the design and tuning of more powerful opto-electronic devices to establish a general method that enables the analysis of the optical response of multi-layer systems. In this section, a transfer matrix method (TMM) for calculating the optical properties of multi-layer systems including constructive and destructive interference will be described.

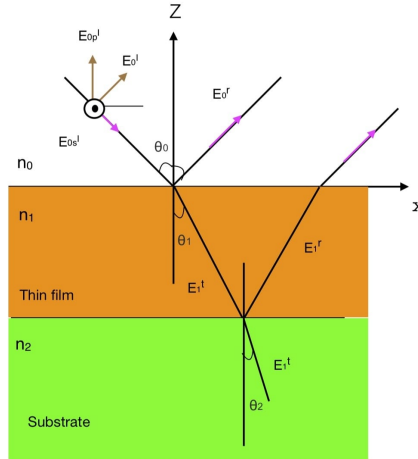


Figure 4.3: Reflection and Transmission at interfaces

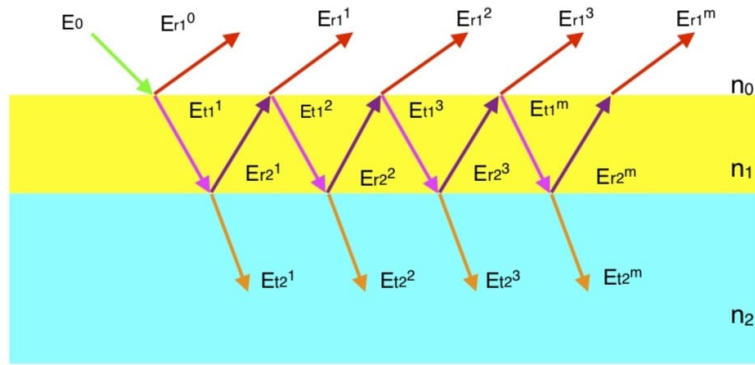


Figure 4.4: Single-layer film on substrate

By writing the field expressions and recognizing their continuity over each boundary, the transfer matrix approach can be extracted. The transfer matrix method is used to solve Maxwell's equations in a multi-layer system subject to a uniform incident field E . Simple matrix operations that connect the top and bottom electric and magnetic fields of a single layer are used in this process.

Fresnel equations derived in the previous section are used to define light reflections for a single interface. Now for multi-layers systems, the powerful TMM will be used for the study of the propagation of light. We will first find the characteristic matrix including coefficients for each layer, and then we will derive the reflectance R for the matrices product of individual layers.

4.3.1 Transfer Matrix for a single layer-film on a substrate

The method of Transfer Matrix can model the reflectance and propagation of light propagating a medium by establishing Maxwell's equations and applying the necessary boundary conditions. In this manner, we are going to use TMM to find the reflectance for a single layer-film on a substrate.

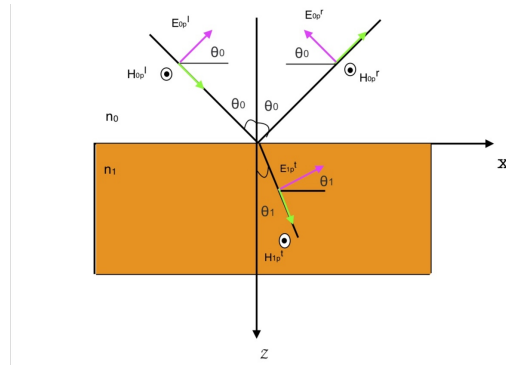


Figure 4.5: Field vectors of incident, reflected and transmitted waves in p- polarization

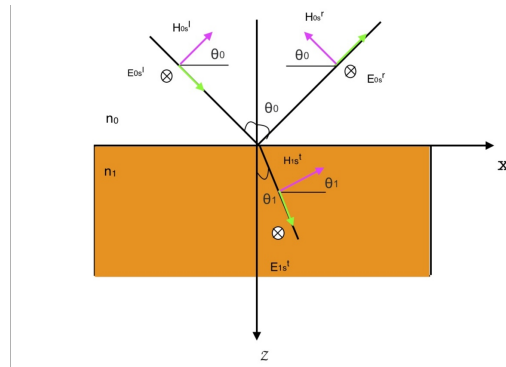


Figure 4.6: Field vectors of incident, reflected and transmitted waves in s- polarization

In figure 4.5 we have:

- An incident plane wave at $z=0$
- xOz plane of incidence
- θ_0 reflection angle
- θ_1 transmission angle
- An interface between two dielectric media of refractive indices n_0 and n_1
- E_{0p}^I and E_{0p}^I the electric vectors' amplitudes arriving at the interface
- E_{0p}^r and E_{0p}^r the reflected electric field vectors
- E_{0p}^t and E_{0p}^t the transmitted electric field vectors

It is known that, Maxwell's equation's electric and magnetic plane wave solutions at a fixed angular frequency take the form:

$$\begin{aligned} E(r, t) &= E_0 e^{i(\omega t \pm k \cdot r)} \\ H(r, t) &= H_0 e^{i(\omega t \pm k \cdot r)} \end{aligned}$$

such that the sign of the scalar product $k \cdot r$ depends on the direction of the wave propagation.

At the interface between mediums n_0 and n_1 , a phase factor must be added for the incident, reflected, and transmitted waves' electric vector which will take the following forms:

$$\begin{aligned} e^{i(\omega t - \frac{2\pi n_0 \sin \theta_0 x}{\lambda} - \frac{2\pi n_0 \cos \theta_0 z}{\lambda})} & \text{ (incident)} \\ e^{i(\omega t - \frac{2\pi n_0 \sin \theta_0 x}{\lambda} + \frac{2\pi n_0 \cos \theta_0 z}{\lambda})} & \text{ (reflected)} \\ e^{i(\omega t - \frac{2\pi n_1 \sin \theta_1 x}{\lambda} - \frac{2\pi n_1 \cos \theta_1 z}{\lambda})} & \text{ (transmitted)} \end{aligned}$$

It is remarkable that Maxwell's equations can be represented in a sinusoidal steady state in terms of a phasor, a complex number representing a sinusoidal function whose amplitude A , angular frequency ω , and initial phase ϕ are time-invariant. Hence, the phasor form of Maxwell's equations in a frequency domain is written as follows:

$$\begin{aligned} \nabla \times \mathbf{E} &= -i\omega\mu\mathbf{H} \\ \nabla \times \mathbf{H} &= i\omega\epsilon\mathbf{E} + \sigma\mathbf{E} \\ \nabla \cdot \mathbf{E} &= 0 \\ \nabla \cdot \mathbf{H} &= 0 \end{aligned} \tag{4.24}$$

where:

- ϵ is the dielectric permittivity
- μ is the magnetic permeability which is taken to be

Applying the curl operator to the electric plane wave solution and comparing to the first equation in the above set of equations, the relation between \mathbf{H} and \mathbf{E} is:

$$\begin{aligned} H &= \sqrt{\frac{\epsilon}{\mu}} \times E \\ H &= \sqrt{\epsilon} K \times E \\ H &= nK \times E \end{aligned} \tag{4.25}$$

where $n = \sqrt{\epsilon}$

The tangential components of the electric field \mathbf{E} and the magnetic field \mathbf{H} that represents the x and y components of the fields are given as:

- for the first medium:

$$\begin{aligned}
E_{0x} &= (E_{0p}^+ e^{-ix_0z} + E_{0p}^- e^{+ix_0z}) \cos \theta_0 \\
E_{0y} &= (E_{0p}^+ e^{-ix_0z} + E_{0p}^- e^{+ix_0z}) \\
H_{0x} &= (-E_{0s}^+ e^{-ix_0z} + E_{0s}^- e^{+ix_0z}) n_0 \cos \theta_0 \\
H_{0y} &= (E_{0p}^+ e^{-ix_0z} - E_{0p}^- e^{+ix_0z}) n_0
\end{aligned} \tag{4.26}$$

- For the second medium :

$$\begin{aligned}
E_{1x} &= E_{1p}^+ e^{-ix_1z} \cos \theta_1 \\
E_{1y} &= E_{1s}^+ e^{-ix_1z} \\
H_{1x} &= -n_1 E_{1s}^+ e^{-ix_1z} \cos \theta_1 \\
H_{1y} &= n_1 E_{1p}^+ e^{-ix_1z}
\end{aligned} \tag{4.27}$$

Knowing that $x_i = \frac{2\pi n_i \cos \theta_i}{\lambda}$.

Therefore, the continuity relation, of the tangential field boundary conditions, derived from Maxwell's equations, should be applied to determine the reflection and transmission of electromagnetic waves through a medium. The continuity equation are:

- For the x tangential component:

$$\begin{aligned}
E_{0x} &= E_{1x} \\
H_{0x} - H_{1x} &= J
\end{aligned} \tag{4.28}$$

- For the y tangential component:

$$\begin{aligned}
E_{0y} &= E_{1y} \\
H_{0y} - H_{1y} &= J
\end{aligned} \tag{4.29}$$

where J is the surface current density.

Equating the tangential components of the electric and magnetic fields using the boundary conditions above and taking $J = 0$ for dielectric materials, we get:

- At $z=0$:

$$\begin{aligned}
E_{0x} &= E_{1x} \\
(E_{0p}^I + E_{0p}^r) \cos \theta_0 &= E_{1p}^t \cos \theta_1 \\
E_{0y} &= E_{1y} \\
E_{0p}^I + E_{0p}^r &= E_{1s}^t \\
H_{0x} &= H_{1x} \\
(-E_{0s}^I + E_{0s}^r) n_0 \cos \theta_0 &= -n_1 E_{1s}^t \cos \theta_1 \\
H_{0y} &= H_{1y} \\
(E_{0p}^I - E_{0p}^r) n_0 &= n_1 E_{1p}^t
\end{aligned} \tag{4.30}$$

- At the plane $z=d$:

$$\begin{aligned}
(E_{1p}^t e^{-ix_1 d} + E_{1p}^r e^{+ix_1 d}) \cos \theta_1 &= E_{2p}^t e^{-ix_2 d} \cos \theta_2 \\
E_{1p}^t e^{-ix_1 d} + E_{1p}^r e^{+ix_1 d} &= E_{2s}^t e^{-ix_2 d} \\
(-E_{1s}^t e^{-ix_1 d} + E_{1s}^r e^{+ix_1 d}) n_1 \cos \theta_1 &= -n_2 E_{2s}^t e^{-ix_2 d} \cos \theta_2 \\
(E_{1p}^t e^{-ix_1 d} - E_{1p}^r e^{+ix_1 d}) n_1 &= n_2 E_{2p}^t e^{-ix_2 d}
\end{aligned} \tag{4.31}$$

Now, we will consider the interface between the k^{th} and $(k+1)^{th}$ layers to generalize the problem. The electric and magnetic fields should satisfy the following conditions:

$$\begin{aligned}
E_k^t + E_k^r &= E_{k+1}^t + E_{k+1}^r \\
H_k^t - H_k^r &= H_{k+1}^t + H_{k+1}^r
\end{aligned} \tag{4.32}$$

Recalling the definitions of $r = \frac{E_{k-1}^r}{E_{k-1}^t}$ and $t = \frac{E_k^t}{E_{k-1}^t}$. Each electric and magnetic field is composed of a p and s polarized components, the Fresnel equations associated with the interface between two media (k and $k+1$ at incidence angle different from zero) are as follows:

$$\begin{aligned}
r_{ks} &= \frac{n_{k-1} \cos \theta_{k-1} - n_k \cos \theta_k}{n_{k-1} \cos \theta_{k-1} + n_k \cos \theta_k} \\
r_{kp} &= \frac{n_k \cos \theta_{k-1} - n_{k-1} \cos \theta_k}{n_k \cos \theta_{k-1} + n_{k-1} \cos \theta_k} \\
t_{ks} &= \frac{2n_{k-1} \cos \theta_{k-1}}{n_{k-1} \cos \theta_{k-1} + n_k \cos \theta_k} \\
t_{kp} &= \frac{2n_{k-1} \cos \theta_{k-1}}{n_k \cos \theta_{k-1} + n_{k-1} \cos \theta_k}
\end{aligned} \tag{4.33}$$

Recalling the total reflectance for p and s polarizations:

$$\begin{aligned}
R_{is} &= r_{is} r_{is}^* \\
R_{ip} &= r_{ip} r_{ip}^*
\end{aligned} \tag{4.34}$$

Moreover, for reaching the matrix form we should write equations 4.30 and 4.31 as:

$$\begin{aligned}
E_{k-1}^t &= \frac{e^{i\delta_{k-1}} E_k^t + r_k e^{i\delta_{k-1}} E_k^r}{t_k} \\
E_{k-1}^r &= \frac{r_k e^{-i\delta_{k-1}} E_k^t + e^{-i\delta_{k-1}} E_k^r}{t_k}
\end{aligned} \tag{4.35}$$

where:

- i stands for the two interfaces ($i=1$ for the air-thin film interface and $i=2$ for thin film-substrate interface)
- $\delta_k = \frac{2\pi n_k d_k \cos \theta_k}{\lambda}$ represents phase change of the wave transmitted through the film]

$$\begin{pmatrix} E_{k-1}^t \\ E_{k-1}^r \end{pmatrix} = \frac{1}{t_k} \begin{pmatrix} e^{i\delta_{k-1}} & r_k e^{-i\delta_{k-1}} \\ r_k e^{-i\delta_{k-1}} & e^{-i\delta_{k-1}} \end{pmatrix} \begin{pmatrix} E_k^t \\ E_k^r \end{pmatrix} \quad (4.36)$$

Such that the characteristic matrix of a single layer:

$$M_k = \begin{pmatrix} e^{i\delta_{k-1}} & r_k e^{-i\delta_{k-1}} \\ r_k e^{-i\delta_{k-1}} & e^{-i\delta_{k-1}} \end{pmatrix} \quad (4.37)$$

Where given the reflectance and transmittance for a single film:

$$\begin{aligned} R &= \frac{(E_0^r)(E_0^r)^*}{(E_0^t)(E_0^t)^*} \\ T &= \frac{(E_2^t)(E_2^t)^*}{(E_0^t)(E_0^t)^*} \end{aligned} \quad (4.38)$$

Therefore, to manipulate the above coefficients, we should find the matrices for $k=1$ and $k=2$ for using the matrix in 4.36. For $k=1$:

$$\begin{pmatrix} E_0^t \\ E_0^r \end{pmatrix} = \frac{1}{t_1} \begin{pmatrix} e^{i\delta_0} & r_1 e^{-i\delta_0} \\ r_1 e^{-i\delta_0} & e^{-i\delta_0} \end{pmatrix} \begin{pmatrix} E_1^t \\ E_1^r \end{pmatrix} \quad (4.39)$$

For $k=2$:

$$\begin{pmatrix} E_1^t \\ E_1^r \end{pmatrix} = \frac{1}{t_2} \begin{pmatrix} e^{i\delta_1} & r_2 e^{-i\delta_1} \\ r_2 e^{-i\delta_1} & e^{-i\delta_1} \end{pmatrix} \begin{pmatrix} E_2^t \\ E_2^r \end{pmatrix} \quad (4.40)$$

The relation between transmitted and reflected rays can be derived by combining equations 4.39 and 4.40:

$$\begin{pmatrix} E_0^t \\ E_0^r \end{pmatrix} = \frac{1}{t_1 t_2} \begin{pmatrix} e^{i\delta_1} & r_1 r_2 e^{-i\delta_1} \\ r_1 r_2 e^{-i\delta_1} & e^{-i\delta_1} \end{pmatrix} \begin{pmatrix} E_2^t \\ E_2^r \end{pmatrix} \quad (4.41)$$

We can express the matrix product:

$$(M_1)(M_2) = \begin{pmatrix} a & b \\ c & d \end{pmatrix} \quad (4.42)$$

where using matrix multiplication rules we can find out a , b , c , and d . Thus, the reflectance and transmittance fractions can be written as:

$$\begin{aligned} R &= \frac{cc^*}{aa^*} \\ T &= \frac{(t_1 t_2)(t_1 t_2)^*}{aa^*} \end{aligned} \quad (4.43)$$

4.3.2 Transfer Matrix for a multi-layer thin film

Our job now is to extend the transfer matrix method for a single layer to a multi-layer structure.

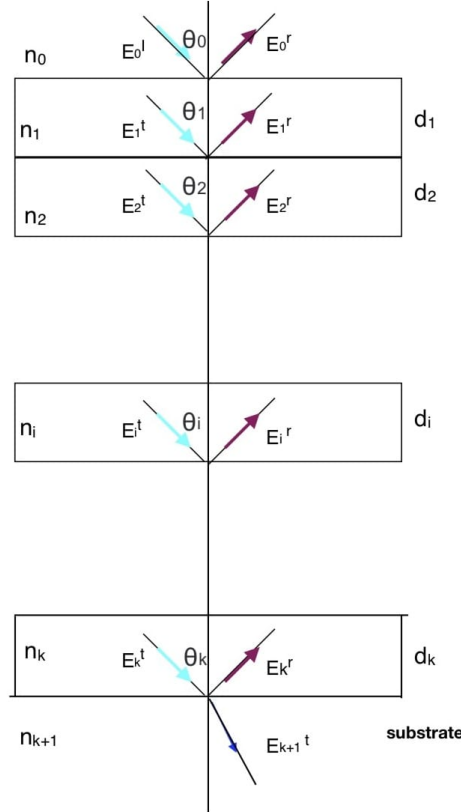


Figure 4.7: The reflectance and transmission through a multi-layer semiconductor

In Fig. 4.7, we consider a stack with parallel-plane layers of indices: $1, 2, \dots, i, \dots, k-1$ that are placed between the first layer and the substrate. Let n_i and d_i be the refractive index and geometrical thickness of the layer i , respectively. We recall Snell's law that relates θ_i with θ_{i+1} :

$$n_i \sin \theta_i = n_{i+1} \sin \theta_{i+1} \quad (4.44)$$

The linear Relation between E_0^t , E_0^r , E_{k+1}^t , and E_{k+1}^r should be provided by the transfer matrix method by applying a characteristic matrix multiplication over the layers. Consequently, the expression for the whole multi-layer structure is developed as:

$$\begin{pmatrix} E_0^t \\ E_0^r \end{pmatrix} = \frac{(M_1)(M_2)\dots(M_{k+1})}{t_1 t_2 \dots t_{k+1}} \begin{pmatrix} E_{k+1}^t \\ E_{k+1}^r \end{pmatrix} \quad (4.45)$$

where

$$\begin{pmatrix} e^{i\delta_{k-1}} & r_k e^{i\delta_{k-1}} \\ r_k e^{-i\delta_{k-1}} & e^{-i\delta_{k-1}} \end{pmatrix} \quad (4.46)$$

and

$$(M_1)(M_2) \dots (M_{k+1}) = \begin{bmatrix} a & b \\ c & d \end{bmatrix} \quad (4.47)$$

Now, we can find out the total response of the above structure by finding out the total reflectance and transmittance:

$$R = \frac{(E_0^r)(E_0^r)^*}{(E_0^t)(E_0^t)^*} = \frac{cc^*}{aa^*} \quad (4.48)$$

$$T = \frac{(t_1 t_2 \dots t_{k+1})(t_1 t_2 \dots t_{k+1})^*}{aa^*}$$

In our research work, we perform the transfer matrix method for a three layers system (air-MnO thin film - silicon). We will Provide a notation for the elements of the matrix that enables expressions relating to the finite number of layers. Thus, we are going to consider an unpolarized light where there is no distinction between the perpendicular and the parallel polarizations. The complex refractive index of the k-1 layer is represented by:

$$n_{k-1}^{\sim} = n_{k-1} + ik_{k-1}^{\sim} \quad (4.49)$$

and that for the k layer is:

$$\tilde{n}_k = n_k + ik_k^{\sim} \quad (4.50)$$

Given the Fresnel coefficients between the k-1 and k layers :

$$r_k = g_k + ih_k \quad (4.51)$$

$$t_k = 1 + r_k = 1 + g_k + ih_k$$

where

$$g_k = \text{real}(r_k) \quad (4.52)$$

$$h_k = \text{imaginary}(r_k)$$

In addition, the phase shift of the $(k-1)^{th}$ layer is expressed as:

$$e^{i\delta_{k-1}} = e^{i2\pi\omega d_{k-1} \cos \theta_{k-1} (n_{k-1} + ik_{k-1}^{\sim})} \quad (4.53)$$

$$e^{i\delta_{k-1}} = e^{\alpha_{k-1}} e^{i\gamma_{k-1}}$$

where

$$\alpha_{k-1} = -2\pi\omega k_{k-1}^{\sim} d_{k-1} \cos \theta_{k-1}$$

$$\gamma_{k-1} = i2\pi\omega n_{k-1}d_{k-1} \cos \theta_{k-1}$$

All the elements of single matrices are complex, so the k^{th} matrix is gives as:

$$M_k = \begin{pmatrix} e^{i\delta_{k-1}} & r_k e^{-i\delta_{k-1}} \\ r_k e^{-i\delta_{k-1}} & e^{-i\delta_{k-1}} \end{pmatrix} \begin{pmatrix} p_k + iq_k & r_k + is_k \\ t_k + iu_k & v_k + iw_k \end{pmatrix} \quad (4.54)$$

We extract the new specified coefficients by applying simple mathematics, as follows:

$$\begin{aligned} p_k &= e^{\alpha_{k-1}} \cos \gamma_{k-1} \\ q_k &= e^{\alpha_{k-1}} \sin \gamma_{k-1} \\ r_k &= e^{\alpha_{k-1}} (g_k \cos \gamma_{k-1} - h_k \sin \gamma_{k-1}) \\ s_k &= e^{\alpha_{k-1}} (h_k \cos \gamma_{k-1} + g_k \sin \gamma_{k-1}) \\ t_k &= e^{-\alpha_{k-1}} (g_k \cos \gamma_{k-1} + h_k \sin \gamma_{k-1}) \\ u_k &= e^{-\alpha_{k-1}} (h_k \cos \gamma_{k-1} - g_k \sin \gamma_{k-1}) \\ v_k &= e^{-\alpha_{k-1}} \cos \gamma_{k-1} \\ w_k &= -e^{-\alpha_{k-1}} \sin \gamma_{k-1} \end{aligned} \quad (4.55)$$

The characteristic matrix product of individual layer matrices should be simplified for the measurement of the reflectance for the multilayer structure of n layers. The recurrence relations make it possible to express the elements of the product matrices in a double suffix form as follows:

$$(M_1)(M_2)\dots(M_{k+1}) = \begin{pmatrix} p_{1,k+1} + iq_{1,k+1} & r_{1,k+1} + is_{1,k+1} \\ t_{1,k+1} + iu_{1,k+1} & v_{1,k+1} + iw_{1,k+1} \end{pmatrix} \quad (4.56)$$

Where the recurrence relations are defined as:

$$\begin{aligned} p_{1,k+1} &= p_{1k}p_{k+1} - q_{1k}q_{k+1} + r_{1k}t_{k+1} - s_{1k}u_{k+1} \\ q_{1,k+1} &= q_{1k}p_{k+1} + p_{1k}q_{k+1} + s_{1k}t_{k+1} + r_{1k}u_{k+1} \\ r_{1,k+1} &= p_{1k}r_{k+1} - q_{1k}s_{k+1} + r_{1k}v_{k+1} - s_{1k}w_{k+1} \\ s_{1,k+1} &= q_{1k}r_{k+1} + p_{1k}s_{k+1} + s_{1k}v_{k+1} + r_{1k}w_{k+1} \\ t_{1,k+1} &= t_{1k}p_{k+1} - u_{1k}q_{k+1} + v_{1k}t_{k+1} - w_{1k}u_{k+1} \\ u_{1,k+1} &= u_{1k}p_{k+1} + t_{1k}q_{k+1} + w_{1k}t_{k+1} + v_{1k}u_{k+1} \\ v_{1,k+1} &= t_{1k}r_{k+1} - u_{1k}s_{k+1} + v_{1k}v_{k+1} - w_{1k}w_{k+1} \\ w_{1,k+1} &= u_{1k}r_{k+1} + t_{1k}s_{k+1} + w_{1k}v_{k+1} - v_{1k}w_{k+1} \end{aligned} \quad (4.57)$$

The reflection would finally have the following expression:

$$R = \frac{cc^*}{aa^*} = \frac{t_{1,k+1}^2 + u_{1,k+1}^2}{p_{1,k+1}^2 + q_{1,k+1}^2} \quad (4.58)$$

We adopted the same strategy derived above in our model, but for unpolarized light. Subsequently, for both the perpendicular and parallel polarizations, the recurrence relations should be determined.

$$\begin{aligned} R_s &= \frac{t_{12s}^2 + u_{12s}^2}{p_{12s}^2 + q_{12s}^2} \\ R_p &= \frac{t_{12p}^2 + u_{12p}^2}{p_{12p}^2 + q_{12p}^2} \end{aligned} \quad (4.59)$$

Where the system's total reflectivity is:

$$R = \frac{1}{2}(R_p + R_s) \quad (4.60)$$

The appropriate Fresnel coefficients are, at the same time, presented as:

$$\begin{aligned} r_p &= \frac{r_{1p} + r_{2p}e^{-2i\delta}}{1 + r_{1p}r_{2p}e^{-2i\delta}} \\ r_s &= \frac{r_{1s} + r_{2s}e^{-2i\delta}}{1 + r_{1s}r_{2s}e^{-2i\delta}} \\ r &= \frac{1}{2}(r_p + r_s) \end{aligned} \quad (4.61)$$

As a summary of our work, the reflectance coefficient is separated into real and imaginary parts: $r(\omega) = A + iB$. Every one of our experimental reflectivity measurements is extrapolated at the low and high frequency end using Origin software. The estimated error for the measured values of reflectivity is about 1% , upon extrapolation , it may reach 20% at the boundaries but remains very small in the middle of the spectrum. The results are put in a Kramers-Kronig MATLAB code that gives the values of $\phi(\omega)$ at every wave number. We obtain: $r(\omega) = \sqrt{R}\exp^{i\phi(\omega)} = \sqrt{R}\cos\phi + \sqrt{R}\sin\phi$. Finally, the two equations are equated as follows:

$$\begin{cases} A - \sqrt{R}\cos\phi = 0 \\ B - \sqrt{R}\sin\phi = 0 \end{cases} \quad (4.62)$$

The only unknowns in this system of two equations are the index of refraction and extinction coefficient of the film which will be obtained by equating these two equations using a MATLAB code that performs iterations on all the frequency range.

4.4 Description of the Analytical Model

In this section, we will describe the steps that were followed in order to develop our computational code to retrieve the complex dielectric properties.

We start by inputting the fixed parameters in the code. Our fixed parameters are the index of refraction of air n_0 , the thickness of the manganese oxide thin film, the wave-number range ω , and the experimental values of the reflectance R . In addition, we add the the incident angle θ_0 , and the values of ϕ that were mentioned in the previous section are also inserted.

We then give a range of values for both n and k . Take n as a row vector and k as a column vector and arrange them in a form of a table, where for every n we have a corresponding k and the values in the table are the multiplication of these n and k .

$k \backslash n$	n_1	n_2	n_3	...
k_1	n_1k_1	n_2k_1	n_3k_1	...
k_2	n_1k_2	n_2k_2	n_3k_2	...
k_3	n_1k_3	n_2k_3	n_3k_3	...
\vdots	\vdots	\vdots	\vdots	\ddots

Figure 4.8: Table sample for the values of n and k

Then we insert the two formulas from Eq. 4.62 individually. The physics behind our code underlies in this step. When inserting the derived equations, we include all the physical properties and the theoretical derivations of the boundary value problem.

We now add two tables each containing a grid of n and k resulting from each formula. These two tables are sorted in ascending order and the position of the smallest value in each column is recorded for both tables. By knowing this position, two sets of values of n and k can be obtained from each table using the step that was given. $n = n_{max} - (step \times position)$. The position is taken with respect to n_{max} . Next, we form another table similar to the ones before but using the new sets of n and k that were obtained. Let $N_1 = n_1 + ik_1$ and

$N_2 = n_2 + ik_2$ be the complex indices of refraction extracted from the first and second table respectively. We apply a condition on N_1 and N_2 to be equal or extremely close to each other, i.e. their difference should be approximately zero. Another condition is introduced which imposes that the calculated reflectance must be equal to the measured experimental reflectance data. This limits our calculations to only one value of n and k for each wave number which when combined, results in the graphs of n and k for every sample.

Chapter 5

RESULTS AND DISCUSSIONS

In this chapter, we use the developed model to retrieve the dielectric function of Manganese Oxide thin films deposited on Silicon substrate using infrared reflectivity measurements.

The amplitudes of the reflected rays are measured using the experimental setup described in chapter 4. Using the Kramers-Kronig conversion theorem, we determined the phases of the plane infrared electromagnetic waves. Then, the complex infrared dielectric function, of Manganese Oxide grown at different conditions using the PLD technique, is deduced using the numerical technique mentioned in chapter 4.

5.1 Measurements

FT-IR measurements were performed on the samples to measure their reflectivity spectra as a function of the excitation wavelength. Then, the phase shift as a function of excitation wavelength is retrieved using the Kramers-Kronig conversion theorem. From the reflectivity \mathbf{R} and the phase shift ϕ , we were able to determine the complex refractive index $(n + ik)$ spectrum for each sample.

The figure below shows the refractive index spectrum as a function of excitation wavelength.

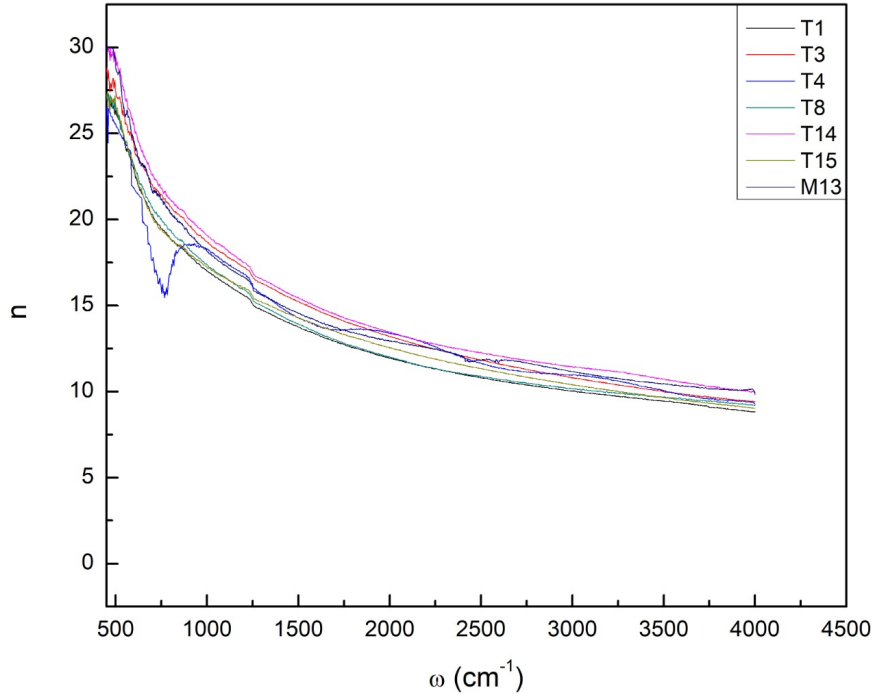


Figure 5.1: Refractive index spectrum as a function of excitation wavelength

A refractive index is an indicator of how different frequencies and wavelengths of light propagate through a transparent material. As shown in Fig.5.1, the material used in our work is of high index of refraction. Thus, our material has high end at infrared, so it can do more reflections. High refractive index materials are increasingly prevalent in optoelectronic applications. They are primarily useful for optimizing the visual properties of electronic displays, including LCDs, OLEDs, and quantum dot (QDLED) televisions.

Thus, the real and imaginary parts of the dielectric functions are then derived from the relationships:

$$\begin{aligned}\epsilon_1(\omega) &= n^2(\omega) - k^2(\omega) \\ \epsilon_2(\omega) &= 2n(\omega)k(\omega)\end{aligned}$$

In the following subsections, we will present the real ϵ_1 and the imaginary ϵ_2 of the dielectric function ϵ as function of ω for the different samples grown at different conditions. In the first subsection, we will investigate the affect of the temperature on ϵ_1 and ϵ_2 whereas in the second subsection we will study the affect deposition pressure on both ϵ_1 and ϵ_2 . In the third subsection, we will see how do ϵ_1 and ϵ_2 behave with changing the laser energy. Lastly, in the fourth subsection we will study the affect of the plasma source on ϵ_1 and ϵ_2 .

5.1.1 Measurements for the samples grown at different temperature

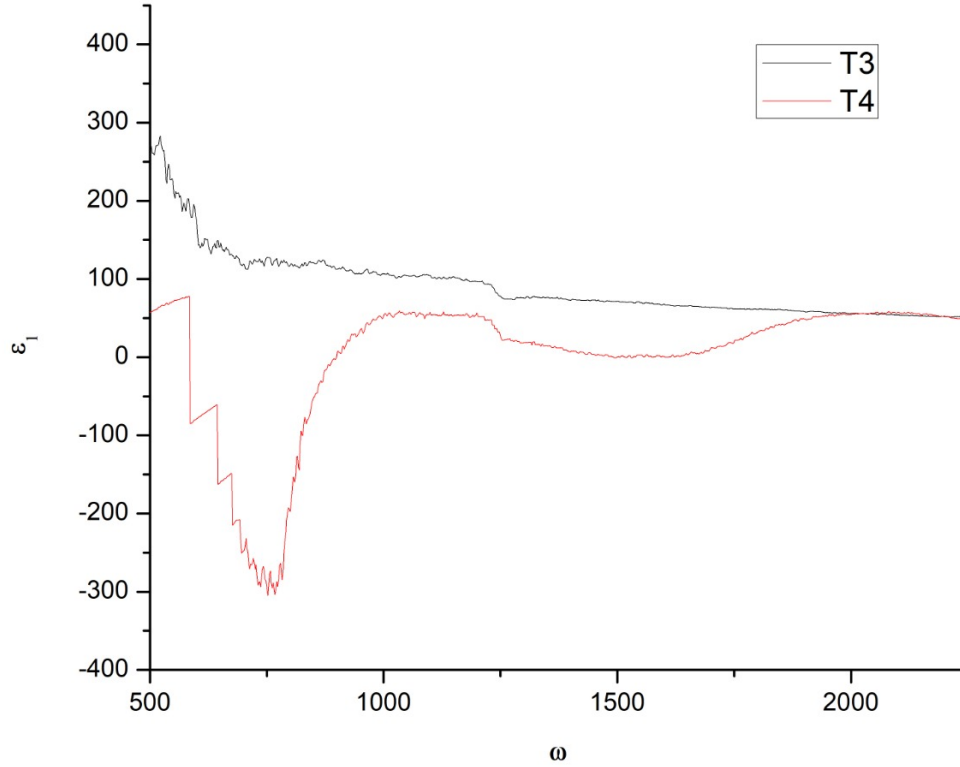


Figure 5.2: Real part of the dielectric function as function of ω for thin film synthesized at different temperature

Fig.5.2 presents the real part of the complex infrared dielectric functions of manganese oxide thin films synthesized at two different temperatures. As shown in Fig.5.2, the real part of the dielectric constant increases with increase in temperature. This phenomenon is explained by using dielectric polarization. At low frequency, four types of polarization occur simultaneously: electronic polarization, ionic polarization, dipolar polarization and interfacial polarization. Nonetheless, the dielectric constant is mostly related to the interfacial polarization. As frequency increases, the interfacial polarization fail to occur and thus dipolar polarization is the main contributor. This also happens to dipolar and atomic polarizations at greater frequencies. At low frequency, the charge carriers reach the grain boundary and accumulated at the boundary resulting in interfacial polarization, yet as frequency increases the dielectric constant decreases

because of the transition from interfacial polarization to dipolar polarization. Interfacial polarization generally takes a longer time to form completely than other polarizations. The dielectric constant increases with increase in temperature. The charge carriers are at low energy state when the temperature is relatively lower. Thus, the charge carriers are difficult to move and the movement to follow the direction of the applied field is relatively small which results in low contribution to polarization and dielectric behaviour. With the increase in temperature, the charge carriers are excited and have enough energy to follow the change of the applied field, therefore increase the dielectric constant.

In Fig.5.2, we can see that sample T4 has negative dielectric constant. At high frequencies, resonance occurs and this indicates a polar behavior of the material.

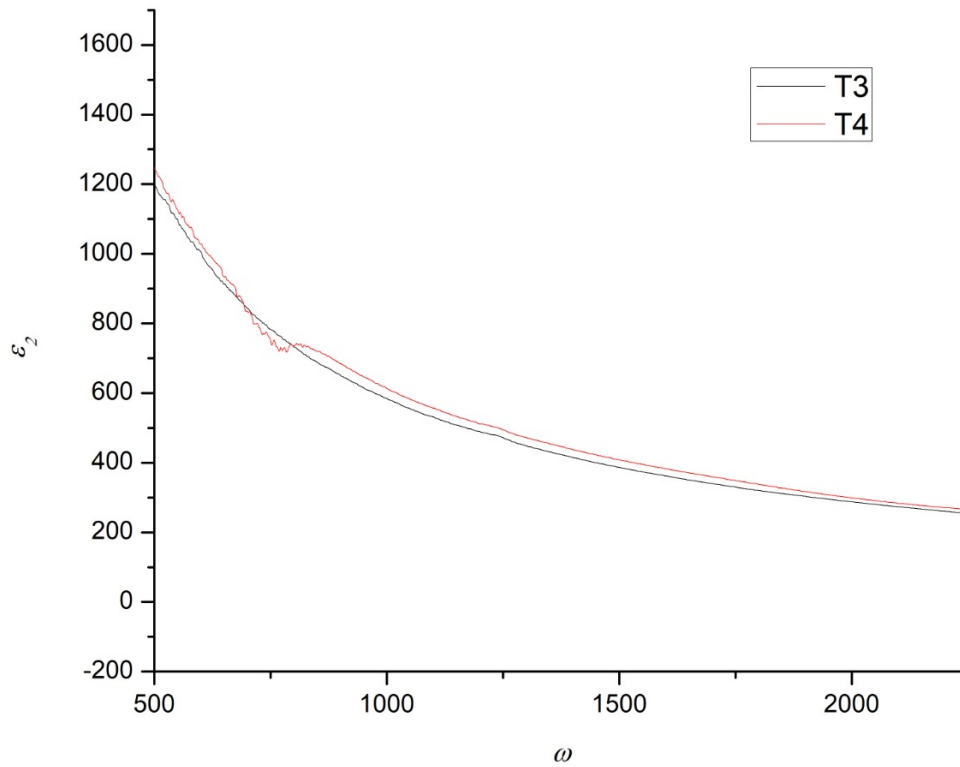


Figure 5.3: Imaginary part of the dielectric function as function of ω for thin film synthesized at different temperature

Fig.5.3 presents the imaginary part of the complex infrared dielectric functions of manganese oxide thin films synthesized at two different temperatures. As shown in Fig.5.3, the imaginary part of the dielectric function is not affected by the change of temperature.

5.1.2 Measurements for the samples grown at different deposition pressure

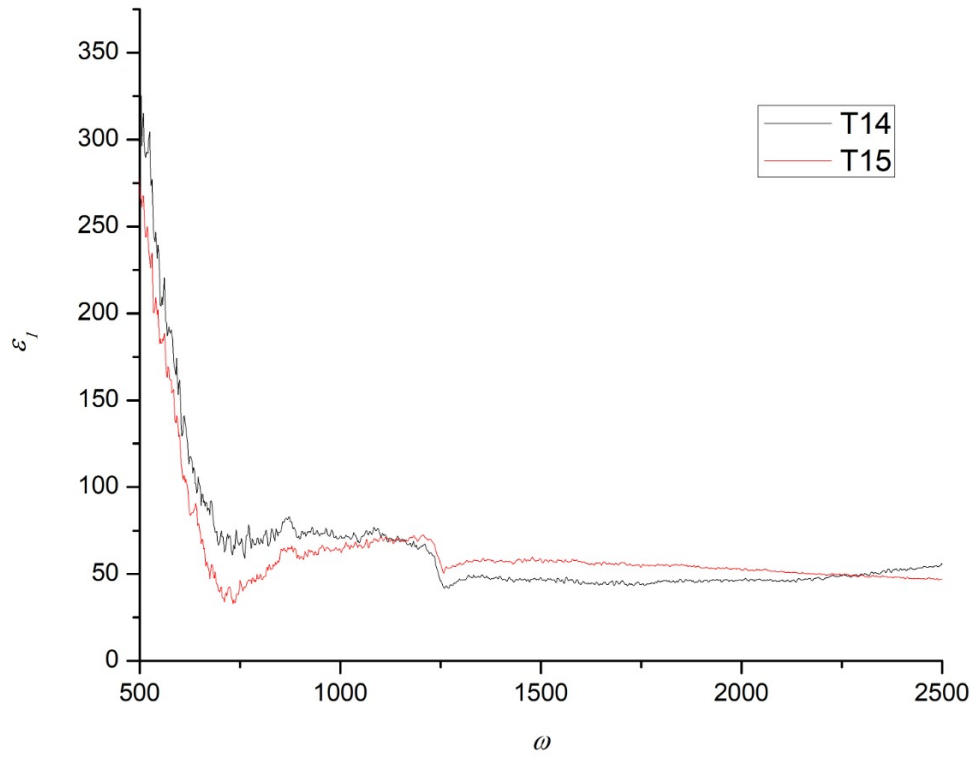


Figure 5.4: Real part of the dielectric function as function of ω for thin film synthesized at different pressure

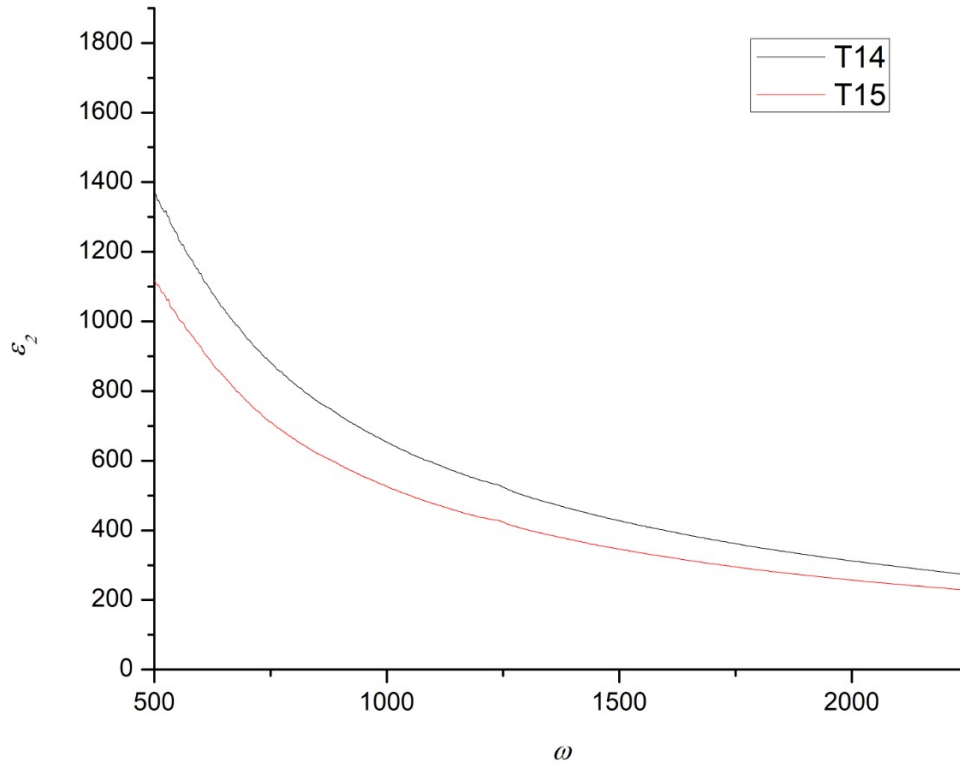


Figure 5.5: Imaginary part of the dielectric function as function of ω for thin film synthesized at different pressure

Fig.5.4 and Fig.5.5 present the real and imaginary parts of the complex infrared dielectric functions of manganese oxide thin films synthesized at two different deposition rates. As shown in Fig.5.4, the real part of the dielectric property is not affected by the change of the deposition rate while the imaginary part of the dielectric property increases with the increase of pressure, as shown in Fig.5.5. This also shows that the samples used are transparent and contain defects.

5.1.3 Measurements for the samples grown at different plasma power

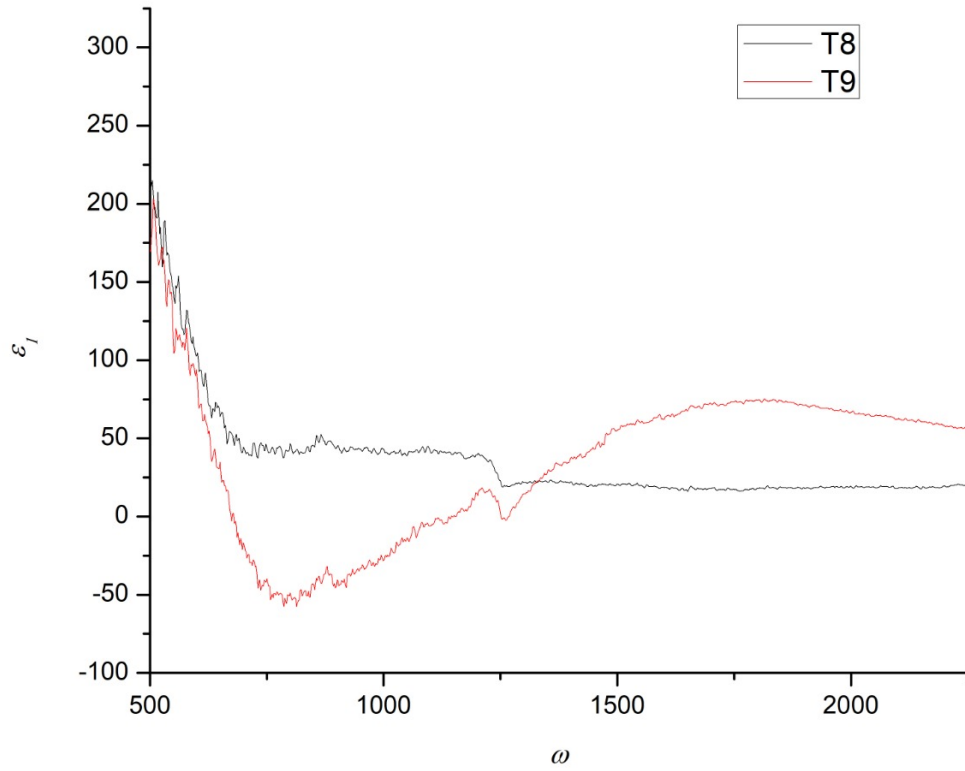


Figure 5.6: Real part of the dielectric function as function of ω for thin film synthesized at different plasma power

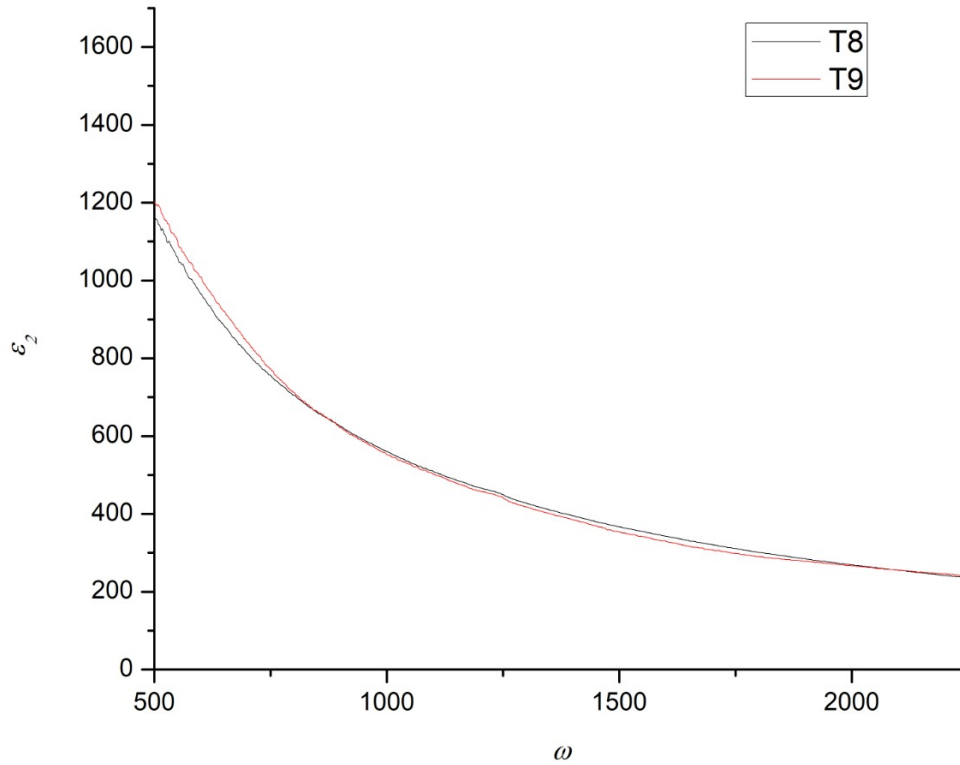


Figure 5.7: Imaginary part of the dielectric function as function of ω for thin film synthesized at different plasma power

Fig.5.6 and Fig.5.7 present the real and imaginary parts of the complex infrared dielectric functions of manganese oxide thin films synthesized at two different plasma source. As shown in Fig.5.6 and Fig.5.7, we can see that plasma power has no effect on the dielectric function.

Both T8 and T9 are synthesized on a high pressure around 250 mTorr. T8 is synthesized with the presence of a plasma source while T9 is synthesized without the presence of a plasma source. The X-ray diffraction measurements of the two samples show that the two samples have the same microstructure of the manganese oxide thin film [1]. This agrees with our obtained results of the dielectric properties.

5.1.4 Measurements for the samples grown at different laser energy

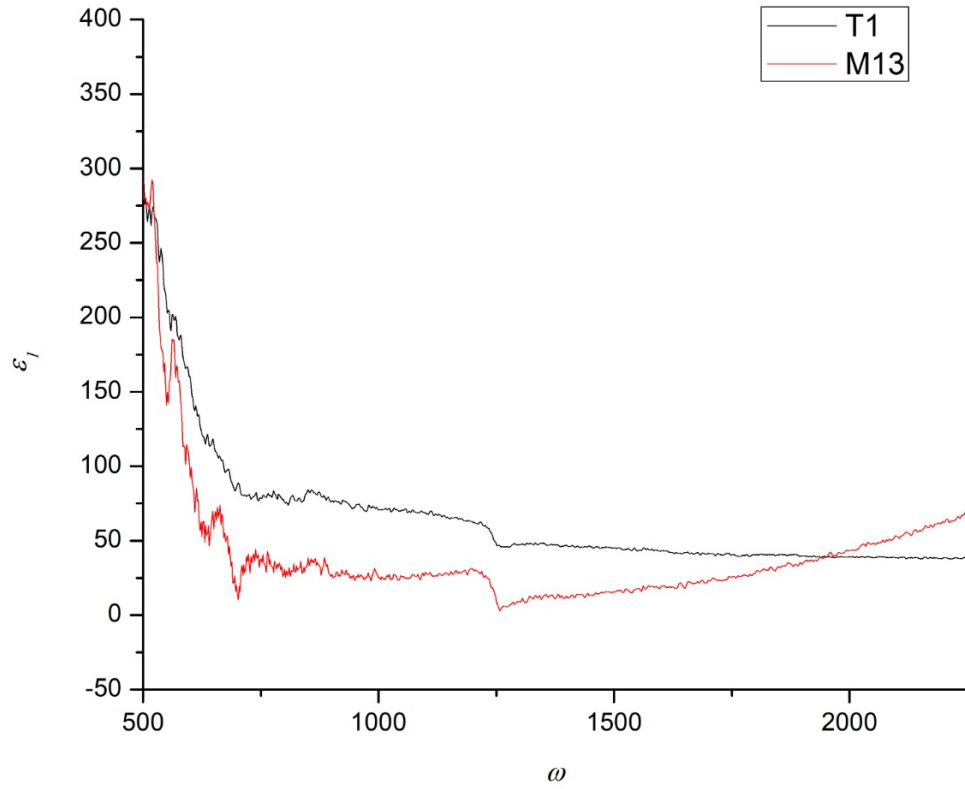


Figure 5.8: Real part of the dielectric function as function of ω for thin film synthesized at different laser energy

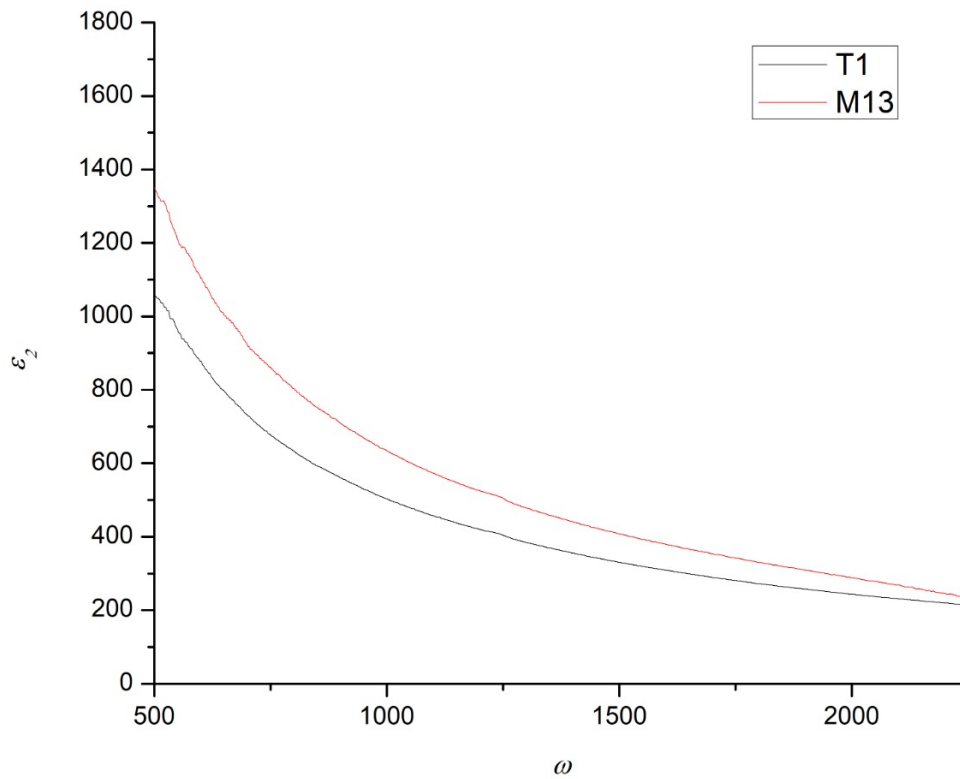


Figure 5.9: Imaginary part of the dielectric function as function of ω for thin film synthesized at different laser energy

Fig.5.10 and Fig.5.11 present the real and imaginary parts of the complex infrared dielectric functions of manganese oxide thin films synthesized at two laser energies. As shown in Fig.5.10, the real part of the dielectric property is not affected by the change of the laser energy while the imaginary part of the dielectric property decreases with the increase of laser energy, as shown in Fig.5.5.

To check that the collected data are reasonable, we recalculate the **reflectance** "R" and the **reflectance** " ϕ " as function of ω . Then, we compare the numerically calculated results with the experimental ones. In the Fig. 5.10 and Fig. 5.11, we display the calculated reflectance R_{cal} and the measured experimental reflectance data R_{exp} as function of ω . Besides, the calculated phase shift ϕ_{cal} and the phase shift determined by Kramers-Kronig equations ϕ_{exp} as function of ω .

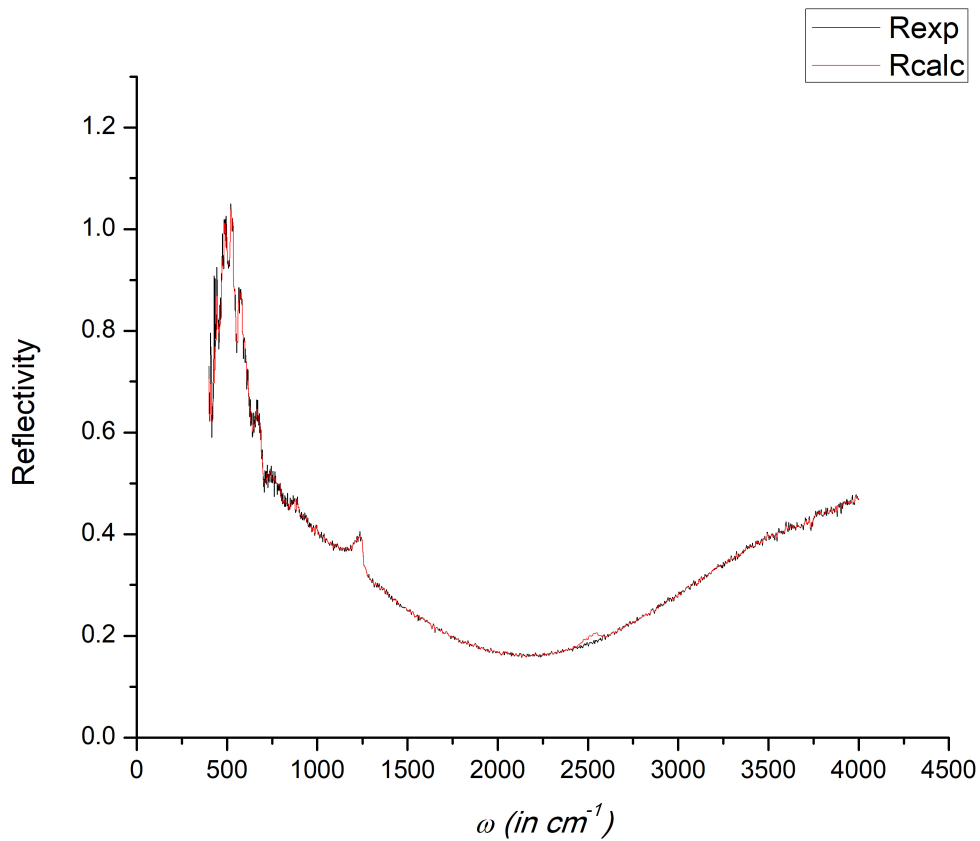


Figure 5.10: Reflectivity measurements as function of ω for sample M13

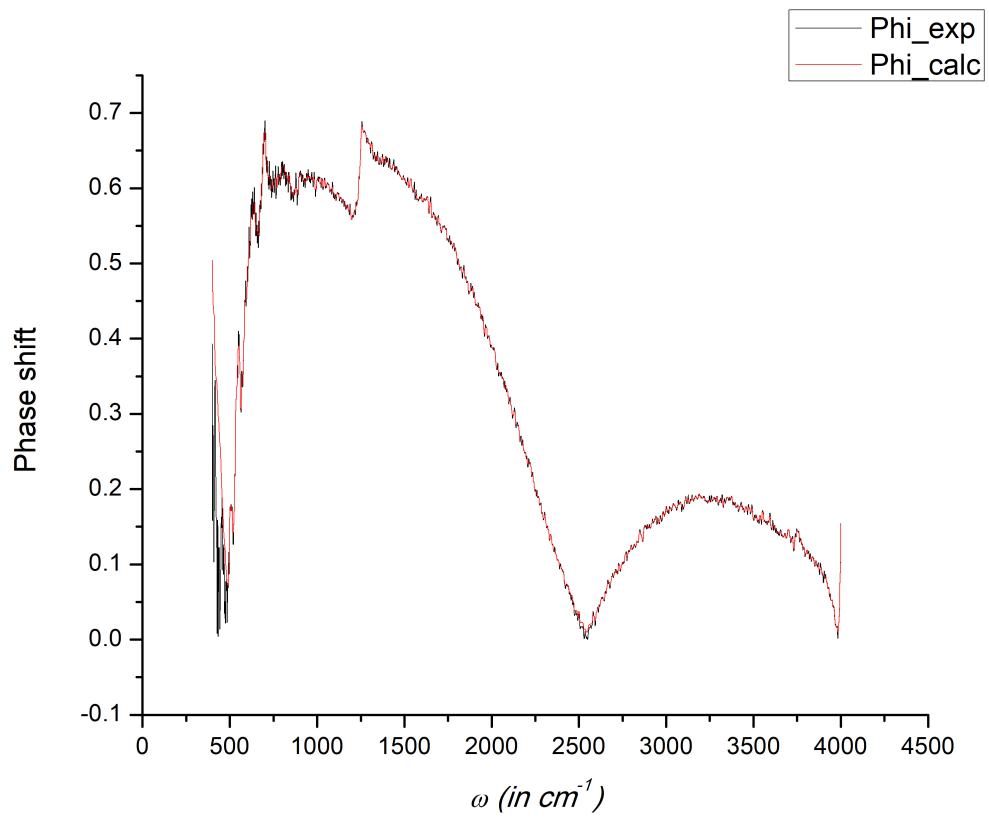


Figure 5.11: Reflectivity measurements as function of ω for sample M13

From Fig. 5.10 and Fig. 5.11, we deduce that the recalculated reflectivity and phase shift agree with the experimental data. Thus, the experimental results are regenerated from the back calculations of the reflectivity and phase shift. Therefore, the estimation of the dielectric properties is true.

Chapter 6

CONCLUSION AND FUTURE WORK

In this work, an experimental technique for the measurement of the index of refraction and the complex infrared dielectric function of different micro-structure of Manganese Oxide thin films deposited on substrate is used.

In chapter 2, we cover Maxwell's theory, as well as the laws governing the propagation of electromagnetic waves in a polar dielectric. The behavior of electric and magnetic fields in dielectrics are described in details. This chapter should provide the necessary information on the interaction between light and matter. Besides, literature review on Manganese Oxide is presented.

In chapter 3, we present the experimental techniques used in this work. We start with a detailed description of the Pulsed Laser Deposition (PLD) growth technique that has been used to synthesis manganese oxide thin films on silicon substrate. In addition, we present the Fourier Transform Infrared Spectrometer (FTIR) used in this work. We also present the characteristics of this technique which make it the tool of choice for probing the complex dielectric functions of materials.

In chapter 4, a detailed theory on the reflection of light from a multilayer system is explained. Then, we describe the transfer matrix method for the calculation of Fresnel coefficients and its application for the evaluation of reflectance. Besides, we illustrate the approach which is based on the combination of Fresnel theory and Kramers-Kronig conversion theorem, for the analysis of the infrared reflectance spectrum of a multilayer system and the derivation of the complex infrared dielectric function of a specific layer of the system.

In chapter 5, we use the technique developed to deduce the complex infrared dielectric function of manganese oxide thin film deposited on silicon substrate at different deposition parameters using the pulsed laser deposition (PLD) growth technique. Firstly, we show that the synthesized manganese oxide are of high index of refraction. Thus, this material can be used as infrared wave guide. Secondly, we check the effect of the growth conditions on the dielectric properties.

We show that the plasma power does not have a significant effect on the dielectric properties of the manganese oxide thin films. However, the real part of the dielectric property increases with the increase of temperature while the imaginary part of the dielectric property increases with the increase of the deposition pressure. On the other hand, the imaginary part of the dielectric property decreases with the increase of the laser energy.

6.1 FUTURE WORK

The most pressing goal of future research to do a full investigation of the microstructure of the film to link the structure to the optical properties for potential technological applications.

Appendix A

Abbreviations

3GPP	Third Generation Partnership Project
AD	Automatic Differentiation
AWGN	Additive White Gaussian Noise
Baron	Branch-And-Reduce Optimization Navigator
BB	Branch and Bound
BFGS	Broyden-Fletcher-Goldfarb-Shanno
BS	Base Station
CCP	Chance-Constraint Programming
CDF	Cumulative Distribution Function
CDMA	Code Division Multiple Access

Bibliography

- [1] Maya Nadim Abi Akl. *Phase Control of Manganese Dioxide Thin Films by Plasma Assisted Laser Ablation*. PhD thesis, American University of Beirut, Department of Physics, 2009.
- [2] Sytle M Antao, Laura A Cruickshank, and Kaveer S Hazrah. Structural trends and solid-solutions based on the crystal chemistry of two hausmannite (Mn_3O_4) samples from the kalahari manganese field. *Minerals*, 9(6):343, 2019.
- [3] R Bowling Barnes, R Robert Brattain, and Frederick Seitz. On the structure and interpretation of the infrared absorption spectra of crystals. *Physical Review*, 48(7):582, 1935.
- [4] Davide Barreca, Alberto Gasparotto, Filippo Gri, Elisabetta Comini, and Chiara Maccato. Plasma-assisted growth of β - MnO_2 nanosystems as gas sensors for safety and food industry applications. *Advanced Materials Interfaces*, 5(23):1800792, 2018.
- [5] VG Bhide and RH Dani. Electrical conductivity in oxides of manganese and related compounds. *Physica*, 27(9):821–826, 1961.
- [6] Lorenzo Bigiani, Dario Zappa, Chiara Maccato, Elisabetta Comini, Davide Barreca, and Alberto Gasparotto. Quasi-1d MnO_2 nanocomposites as gas sensors for hazardous chemicals. *Applied Surface Science*, 512:145667, 2020.
- [7] Eric Cockayne, Igor Levin, Hui Wu, and Anna Llobet. Magnetic structure of bixbyite α - Mn_2O_3 : A combined dft+ u and neutron diffraction study. *Physical Review B*, 87(18):184413, 2013.
- [8] Yilka Dessie, Sisay Tadesse, and Rajalakshmanan Eswaramoorthy. Review on manganese oxide based biocatalyst in microbial fuel cell: Nanocomposite approach. *Materials Science for Energy Technologies*, 3:136–149, 2020.
- [9] Yuming Dong, Hongxiao Yang, Kun He, Shaoqing Song, and Aimin Zhang. β - MnO_2 nanowires: a novel ozonation catalyst for water treatment. *Applied Catalysis B: Environmental*, 85(3-4):155–161, 2009.

- [10] Sophie Fritsch and Alexandra Navrotsky. Thermodynamic properties of manganese oxides. *Journal of the American Ceramic Society*, 79(7):1761–1768, 1996.
- [11] P Gao, Z Chen, TA Tyson, T Wu, KH Ahn, Z Liu, R Tappero, SB Kim, and S-W Cheong. High-pressure structural stability of multiferroic hexagonal Rmno_3 ($\text{R} = \text{Y, Ho, Lu}$). *Physical Review B*, 83(22):224113, 2011.
- [12] S Geller. Structure of $\alpha\text{-Mn}_2\text{O}_3$, $(\text{Mn}^{0.983}\text{Fe}^{0.017})_2\text{O}_3$ and $(\text{Mn}^{0.37}\text{Fe}^{0.63})_2\text{O}_3$ and relation to magnetic ordering. *Acta Crystallographica Section B: Structural Crystallography and Crystal Chemistry*, 27(4):821–828, 1971.
- [13] L. W. Guo, D. L. Peng, H. Makino, Takashi Hanada, S. K. Hong, K. Sumiyama, T. Yao, and K. Inaba. Structural characteristics and magnetic properties of MnO_2 films grown by plasma-assisted molecular beam epitaxy. *Journal of Applied Physics*, 90(1):351–354, July 2001.
- [14] Jiangbo Huo, Guoce Yu, and Jianlong Wang. Efficient removal of Co^{2+} and Sr^{2+} from aqueous solution using polyvinyl alcohol/graphene oxide/ MnO_2 composite as a novel adsorbent. *Journal of Hazardous Materials*, page 125117, 2021.
- [15] Alireza Kashir. *Strain Engineering of Lattice Dynamics and Spin-Phonon Interaction in Rocksalt Magnetic Binary Oxides*. PhD thesis, 12 2019.
- [16] Tommie W Kelley, Paul F Baude, Chris Gerlach, David E Ender, Dawn Muyres, Michael A Haase, Dennis E Vogel, and Steven D Theiss. Recent progress in organic electronics: Materials, devices, and processes. *Chemistry of Materials*, 16(23):4413–4422, 2004.
- [17] Yassine Manane and Rachid Yazami. Accurate state of charge assessment of lithium-manganese dioxide primary batteries. *Journal of Power Sources*, 359:422–426, 2017.
- [18] Toshiro Maruyama and Susumu Arai. Electrochromic properties of cobalt oxide thin films prepared by chemical vapor deposition. *Journal of the Electrochemical Society*, 143(4):1383, 1996.
- [19] PP Paskov. Refractive indices of InSb , InAs , GaSb , $\text{InAs}_{1-x}\text{Sb}_x$, and $\text{In}_{1-x}\text{Ga}_x\text{Sb}$: effects of free carriers. *Journal of applied physics*, 81(4):1890–1898, 1997.
- [20] Michael Pozin and Steven Wicelinski. Safety aspects of lithium primary batteries. In *Electrochemical Power Sources: Fundamentals, Systems, and Applications*, pages 83–111. Elsevier, 2019.

- [21] M Regulski, R Przeniosło, I Sosnowska, D Hohlwein, and R Schneider. Neutron diffraction study of the magnetic structure of α - Mn_2O_3 . *Journal of alloys and compounds*, 362(1-2):236–240, 2004.
- [22] DM Roessler. Kramers-kronig analysis of reflection data. *British Journal of Applied Physics*, 16(8):1119, 1965.
- [23] Kailash K Sharma. *Optics: principles and applications*. Elsevier, 2006.
- [24] John Strong and RT Brice. Optical properties of magnesium oxide. *JOSA*, 25(7):207–210, 1935.
- [25] SK Tripathy. Refractive indices of semiconductors from energy gaps. *Optical materials*, 46:240–246, 2015.
- [26] M Claudia Troparevsky, Adrian S Sabau, Andrew R Lupini, and Zhenyu Zhang. Transfer-matrix formalism for the calculation of optical response in multilayer systems: from coherent to incoherent interference. *Optics express*, 18(24):24715–24721, 2010.
- [27] Zhong-Shuai Wu, Wencai Ren, Da-Wei Wang, Feng Li, Bilu Liu, and Hui-Ming Cheng. High-energy MnO_2 nanowire/graphene and graphene asymmetric electrochemical capacitors. *ACS nano*, 4(10):5835–5842, 2010.
- [28] Mao-Wen Xu, Wei Jia, Shu-Juan Bao, Zhi Su, and Bin Dong. Novel mesoporous MnO_2 for high-rate electrochemical capacitive energy storage. *Electrochimica Acta*, 55(18):5117–5122, 2010.
- [29] Sangmoon Yoon, Seoung-Hun Kang, Sangmin Lee, Kuntae Kim, Jeong-Pil Song, Miyoung Kim, and Young-Kyun Kwon. A “non-dynamical” way of describing room-temperature paramagnetic manganese oxide. *Physical Chemistry Chemical Physics*, 21(29):15932–15939, 2019.
- [30] Zheng Zhang and Yuanhui Ji. Nanostructured manganese dioxide for anticancer applications: preparation, diagnosis, and therapy. *Nanoscale*, 12(35):17982–18003, 2020.
- [31] Lei Zhou, Chunyang Li, Xiang Liu, Yusong Zhu, Yuping Wu, and Teunis van Ree. Metal oxides in supercapacitors. In *Metal Oxides in Energy Technologies*, pages 169–203. Elsevier, 2018.